Title: Variations of intracellular density during the cell cycle arise from tip-growth regulation in fission yeast

Short title: Density variations during the fission yeast cell cycle

Authors: Pascal D. Odermatt[1,2], Teemu P. Miettinen[3,4], Joon Ho Kang[3,5,6], Emrah Bostan[7], Scott Manalis[3,8,9], Kerwyn Casey Huang[2,10,11,*], Fred Chang[1,*]

[1]Department of Cell and Tissue Biology, University of California, San Francisco, San Francisco, CA 94143, USA

[2]Department of Bioengineering, Stanford University, Stanford, CA 94305, USA

[3]Koch Institute for Integrative Cancer Research, Massachusetts Institute of Technology, Cambridge, MA 02139, USA

[4]MRC Laboratory for Molecular Cell Biology, University College London, London, UK

[5]Department of Physics, Massachusetts Institute of Technology, Cambridge, MA 02139, USA

[6]Brain Science Institute, Korea Institute of Science and Technology, Seoul 02792, South Korea

[7]Informatics Institute, University of Amsterdam, 1098 XH Amsterdam, Netherlands

[8]Department of Biological Engineering, Massachusetts Institute of Technology, Cambridge, MA 02139, USA

[9]Department of Mechanical Engineering, Massachusetts Institute of Technology, Cambridge, MA, 02139, USA.

[10]Department of Microbiology and Immunology, Stanford University School of Medicine, Stanford, CA 94305, USA

[11]Chan Zuckerberg Biohub, San Francisco, CA 94158, USA

*Contact: kchuang@stanford.edu and fred.chang@ucsf.edu

Keywords: quantitative phase imaging, fission yeast, *Schizosaccharomyces pombe*, dry-mass density, cell-cycle arrest, cytokinesis, mitosis

Abstract

Intracellular density impacts the physical nature of the cytoplasm and can globally affect cellular processes, yet density regulation remains poorly understood. Here, using a new quantitative phase imaging method, we determined that dry-mass density varies during the cell cycle in fission yeast. Density decreased during G2, increased in mitosis and cytokinesis, and rapidly dropped at cell birth. These density variations were explained by a constant rate of biomass synthesis, coupled to slowdown of volume growth during cell division and rapid expansion post-cytokinesis. Arrest at specific cell-cycle stages led to continued increases or decreases in density. Spatially heterogeneous patterns of density suggested links between density regulation and tip growth, and septum bending away from higher-density daughters linked density to intracellular osmotic pressure. Our results demonstrate that systematic density variations during the cell cycle are predominantly due to modulation of volume expansion, and reveal functional consequences of density gradients and cell-cycle arrests.

Introduction

Intracellular density, a cumulative measure of the concentrations of all cellular components, is an important parameter that globally affects cellular function: density affects the concentration and activities of biomolecules, and can impact biophysical properties of the cytoplasm such as macromolecular crowding, diffusion, mechanical stiffness, and phase transitions (1-4). Although it is often assumed that density must be maintained at a particular level to optimize fitness, there is a growing appreciation that intracellular density often varies across physiological conditions. For example, substantial shifts in density and/or crowding have been detected in development, aging, and disease states (3, 5). Even normal cell-cycle progression can involve changes in density; in cultured mammalian cells, volume increases by 10-30% during mitosis (6, 7), which likely dilutes the cytoplasm prior to an increase in density during cytokinesis.

Despite this biological centrality, the homeostatic mechanisms maintaining cellular density remain poorly understood. Over the course of a typical cell cycle, cells both double their volume and duplicate all cellular contents. A critical unresolved question is how this growth in cell volume (increase in cell size) and biosynthesis are coordinated. In walled cells, the rate of volume growth is dictated largely by cell-wall synthesis and turgor pressure (8). In principle, feedback mechanisms could tightly couple biosynthesis with wall expansion. However, recent studies have demonstrated that it is possible to decouple biosynthesis from volume growth. For instance, budding yeast cells that are arrested in G1 phase grow to very large sizes and exhibit dilution of the cytoplasm accompanied by decreased protein synthesis and growth rate (9). Conversely, temporary inhibition of volume growth using osmotic oscillations or inhibition of secretion leads to increased density accompanied by a subsequent dramatic increase in volume growth rate in fission yeast (10).

68

69 Numerous methods have been developed to measure aspects of biomass and intracellular
70 density and crowding in living cells (2, 3, 11). Suspended microchannel resonators (SMRs) infer
71 buoyant cell mass from changes in the frequency of a resonating cantilever as a single cell passes
72 through an embedded microchannel (12). As an alternative to SMRs, quantitative phase imaging
73 (QPI) is a well-established optical technique for extracting dry-mass measurements from
74 changes in the refractive index (13). The interpretation of phase shifts depends on the similarity
75 in the refractive indices of major cellular components such as proteins, lipids, and nucleic acids
76 (11). Previous studies have used phase gratings or holography to generate phase-shift maps that
77 can be used to quantify intracellular density; these approaches require specialized equipment
78 (14). Precise measurement of density throughout the cell cycle requires non-invasive, long-term
79 quantification of single cells at high spatial and temporal resolution.

80

81 Here, we developed a new QPI method for measuring the intracellular density of fission yeast
82 cells. This label-free method is based on the analysis of *z*-stacks of brightfield images (15), thus
83 having the advantage of not requiring a specialized phase objective or holographic system. The
84 fission yeast *Schizosaccharomyces pombe* is a leading cell-cycle model, as these rod-shaped cells
85 have a highly regular shape, size, and cell cycle conducive to quantitative analyses. Using QPI to
86 track the density of individual cells as they grew and divided within a microfluidic chamber, we
87 determined that wild-type fission yeast cells exhibit characteristic density changes during the
88 cell cycle, in which density falls during G2 phase and increases during mitosis and cytokinesis.
89 These density variations arise from differences in the relative rates of volume and mass growth;
90 while mass grows exponentially throughout the cell cycle, volume growth varies dependent on
91 cell cycle stage/phase. Perturbations to cell-cycle progression and/or growth exacerbated

density changes. We further observed gradients in density within single cells and found that intracellular density variations were correlated with tip growth and intracellular pressure. Our findings illustrate a general mechanism by which density is regulated through controlling the relative rates of volume growth and biosynthesis.

Results

QPI enables high-resolution measurements of intracellular density in growing cells

To measure intracellular density using a standard wide-field microscope, we developed a version of QPI in which the phase shift is retrieved computationally from a *z*-stack of brightfield images (15). This label-free approach takes advantage of the relationship between the intracellular concentration of biomolecules and the refractive index of the cell interior (11), which can be computed from the light intensity profile along the *z*-direction using the transport-of-intensity equation (Figure 1A, Methods). To calibrate phase shifts with absolute concentrations (dry-mass/volume), we measured the phase shifts within cells grown in media containing a range of concentrations of a calibration standard (bovine serum albumin, BSA) (Methods); these measurements showed a linear relationship that can be used to extrapolate the intracellular density of cells (Figure 1B). This method provides pixel-scale measurements of density in living cells and can easily be applied during time-lapse imaging with sub-minute time resolution on most wide-field microscopes.

Using this methodology, we determined that the mean dry-mass density of an asynchronous population of wild-type *S. pombe* cells growing at 30 °C in rich YE5S medium was 282±16 mg/mL (Figure 1C). The distribution of densities was remarkably narrow, with a coefficient of variation (CV) of 0.06, despite variability in cell size, cell-cycle stage, and various sources of intracellular heterogeneities such as lipid droplets (Figure S1) and cell-wall septa (both of which were regions of high signal, Figure 1A). For cells within the same cell-cycle stage, the distribution of densities was even more narrow (CV<0.05, Figure S1B). The nucleus was not distinguishable in most phase-shift maps, indicating similar density as the cytoplasm (Figure 1A). A similar distribution

120 of densities was observed in cells grown at 25 °C and after temperature shifts (Figure 1D).
121 Together, these results suggest that dry-mass density is robustly maintained, and demonstrate
122 that this QPI approach can precisely measure absolute dry-mass density in living cells with high
123 temporal and spatial resolution.
124
125 **Intracellular density follows a characteristic trajectory during the *S. pombe* cell cycle**
126 To determine whether intracellular density changes over the course of the fission yeast cell cycle,
127 we imaged proliferating cells in time-lapse using QPI in a microfluidic device under constant flow
128 of growth medium (Methods; Figure 2A, Movie S1). Density maps were segmented to extract
129 cellular dimensions, from which volume was computed (Methods; Figure 1A). Total dry mass of
130 each cell was computed from volume and mean density measurements. We imaged cells
131 throughout their entire cell cycle, and then aligned the computed data from each cell by relative
132 cell-cycle progression, from cell birth (first detectable physical separation between daughter
133 cells) until just before cell-cell separation at the end of the cell cycle. As observed previously
134 (16), cells exhibited steady tip growth in interphase (mostly G2 phase), and then volume growth
135 slowed or halted during mitosis and cytokinesis (defined here as the period starting from
136 septum formation and ending at daughter-cell separation; Figure 2B).
137
138 Intracellular density displayed consistent dynamics during the *S. pombe* cell cycle. Density
139 gradually decreased from the beginning of the cell cycle through G2 phase by ~5%, followed by a
140 steady rise during mitosis and cytokinesis (Figure 2C). We confirmed these findings using a
141 complementary approach for measuring density. Holographic imaging (Methods) showed that
142 the mean refractive index of cells decreased with cell length prior to septation, whereas cells of
143 similar length with a septum exhibited higher refractive indices (Figure S2A,B) (17). We used a

144 suspended microchannel resonator (SMR) to measure the buoyant mass of single cells in two
145 different density solutions and thereby derive single-cell buoyant densities and volumes (18)
146 (Methods). SMR measurements revealed that fission yeast exhibit a mean buoyant density of
147 1.108±0.005 g/mL, and buoyant densities were lower in intermediate-sized cells than in small
148 and large cells (Figure 2D, S2C,D), consistent with our QPI-based observations of cell cycle-
149 dependent densities (Figure 2C, S2E). As expected, the relative changes in buoyant density were
150 much less than changes in dry-mass density due to the different nature of the respective
151 measurements: dry-mass density accounts only for a fraction of buoyant density as cells are
152 comprised mostly of water mostly, and hence relative changes are magnified (19).
153
154 We also identified an additional change in density at cell birth. At the end of cytokinesis, the
155 middle layer of the septum is digested, and daughter cells separate (20, 21). During this 5-10-
156 min period, the septum bulges outward on each side to form the rounded shape of the new end,
157 in a physical process driven by turgor pressure (22). QPI analysis of individual cells showed a
158 consistent drop in density within a 5-min window around cell separation (Figure 2E, S3); during
159 this period, cell volume increased by ~5% while density decreased by ~5% (Figure 2E). The
160 magnitude and rapidity of the density change suggest that the volume increase at cell separation
161 is due primarily to swelling from water uptake. Thus, density appears to be directly tied to the
162 dynamics of volume expansion.
163
164 Our precision measurements of cellular dimensions and intracellular density provide a
165 quantitative characterization of dry-mass dynamics (biosynthesis) throughout the cell cycle. The
166 absolute rate of dry-mass accumulation steadily increased during the cell cycle (Figure 2F). Dry-
167 mass dynamics were more exponential than linear in nature (Figure 2G, S4A), as shown by a

168 comparison of linear versus exponential fits (Figure 2G) and in the dynamics of normalized mass
169 growth (Figure S4A). The absolute rate of mass synthesis was therefore higher during mitosis
170 and cytokinesis than at the beginning of the cell cycle, even though the cell slowed in volume
171 growth late in the cycle. Thus, mass production was not tightly coupled to volume growth. These
172 measurements suggest a simple model in which the increase of density in mitosis and cytokinesis
173 arises as consequence of continued mass accumulation when volume growth is halted.
174

175 **Cell-cycle perturbations exacerbate cell cycle-dependent density variation**

176 Our data demonstrate that intracellular density increases during mitosis and cytokinesis as a
177 result of biosynthesis continuing unabated while volume growth slows; conversely, density
178 decreases during interphase because the rate of volume growth surpasses the rate of mass
179 synthesis. However, the origin of these dynamics remains unresolved. One possibility is that the
180 relative rates of mass synthesis and volume growth are not directly coupled; with mass growing
181 exponentially, density variations then arise indirectly as a consequence of cell-cycle regulation of
182 volume expansion, which is controlled by cell polarity programs that redirect the cell wall
183 growth machinery to the middle of the cell for septum formation prior to cytokinesis (23-25).
184 Alternatively, the density at each cell-cycle stage could be directly programmed to specific levels
185 by specific cell-cycle regulators. Another possibility is that density variations may be due to a cell
186 cycle-independent oscillator, such as a metabolic oscillator (26). To distinguish these models, we
187 examined the consequences of arresting or delaying cells at particular stages of the cell cycle
188 (Figure 3A). If there is no strict control of biosynthesis, then when mitosis or cytokinesis is
189 blocked, mass should continue to accumulate and density should reach higher levels than in
190 normal cells, and conversely density should fall below normal in extended interphase. If density
191 is instead regulated at specific levels according to cell-cycle phase, density levels should not

192 change during cell-cycle delays beyond the ranges appropriate for each phase. If a cell cycle-
193 independent oscillator governs density variations, then oscillations could continue even during
194 cell-cycle arrests (27, 28).
195
196 First, we tested whether density would decrease further in *S. pombe* cells experiencing an
197 extended period of growth during interphase. We delayed cells harboring a *cdc25-22* mutation
198 (29) in G2 phase by shifting them from room temperature to the semi-permissive temperature
199 (32 °C). These cells continued to grow from their tips and formed abnormally elongated cells
200 (Figure 3B,C) before dividing. To focus on cells that remained in G2 phase for an extended
201 interval, we limited our analysis to cells that elongated to >2.5-fold their initial length. In these
202 mutant cells, during their prolonged G2 phase of 2-3 h, intracellular density decreased further
203 than in wild-type cells (~8% in *cdc25-22* cells from 267±19 to 245±6 mg/mL, compared to ~5%
204 in wild-type cells from 267±11 to 250±6 mg/mL) (Figure 3C). No evidence of density oscillations
205 in the prolonged G2 phase was evident, arguing against cell-cycle independent oscillations as the
206 cause of density variations during a normal cell cycle. These data suggest that density falls during
207 G2 phase because the rate of volume growth continues to be slightly faster than the rate of
208 biosynthesis.
209
210 Second, we tested whether cells arrested in mitosis displayed increased intracellular density
211 (Figure 4A). We delayed cells in metaphase using a *cut7-ts* mutant (kinesin-5) defective in
212 mitotic spindle assembly (30). Using QPI, we tracked intracellular density from mitosis initiation
213 until the earliest signs of septum formation. As expected, at the non-permissive temperature this
214 interval was longer for *cut7-ts* cells (20-30 min) than for wild-type cells (10-20 min; Figure
215 4B,C). During this mitotic period, the density of wild-type and *cut7-ts* cells increased at a similar

216 rate (Figure 4B,C): hence, the extended time in metaphase in *cut7-ts* cells led to a greater density
217 increase (7% in *cut7-ts* from 270±12 to 288±14 mg/mL versus 5% in wild-type cells from
218 264±11 to 278±13 mg/mL).
219
220 Third, we arrested cells in cytokinesis, again to test for an increase in density (Figure 4A). *cdc16-*
221 *116* mutant cells arrest in cytokinesis, and thus repeatedly make septa without elongating (31).
222 Upon a shift from 25 °C to the non-permissive temperature (34 °C), cells that maintained
223 cytokinetic arrest continued to increase in cytoplasmic density; density after 90 min was 20-30%
224 higher than in cytokinesis-competent wild-type cells (Figure 4D,E). Thus, biosynthesis continues
225 throughout an extended block of mitosis or cytokinesis, leading to abnormally high intracellular
226 density.
227
228 Finally, we asked whether inhibition of volume growth is sufficient to increase cytoplasmic
229 density. We previously showed that two treatments that slow volume growth (osmotic
230 oscillations and treatment with brefeldin A) led to an increase in cytoplasmic density (10).
231 However, since these treatments do not completely halt volume growth and/or result in cell
232 death, we treated wild-type cells with the F-actin inhibitor latrunculin A, which causes
233 immediate cessation of tip growth independent of cell-cycle stage (32, 33). QPI density maps
234 showed that latrunculin A treatment caused all cells to immediately halt tip growth and begin to
235 steadily increase in density, regardless of cell-cycle stage (Figure 5A,B). The mean density
236 increase after 1 h was ~20% (Figure 5B). Similar increases in density were seen in cells of
237 different sizes (Figure S5). However, we noted that in contrast to the mitotic and cytokinesis
238 arrests, mass increases were variable and on average increased more slowly during latrunculin A

239 treatment than during normal growth (Figure 2F), suggesting a partial slowdown in biosynthesis
240 and/or an increase in degradation.
241
242 Taken together, these results show that cell density differences are exacerbated during cell cycle
243 arrests and that inhibition of volume growth is sufficient to increase intracellular density. These
244 findings are not consistent with models in which density is set at cell-cycle stage-specific levels
245 or involving cell cycle-independent oscillators. Rather, our results strongly support a model in
246 which the variations in intracellular density arise from cell cycle-dependent changes in volume
247 growth rate.
248
249 **A polarized density gradient is associated with the pattern of tip growth**
250 Fission yeast have a well-known pattern of volume growth in which after cell division, the old
251 end initiates tip growth soon after cell birth, and partway through G2, tip growth at the new end
252 begins, but at a slower rate than the old end (16, 34). As expected, our time-lapse data showed
253 that the old and new ends grew over the course of the cycle on average by ~4 and 2 μm,
254 respectively. In QPI density maps, we noted that many cells exhibited a gradient of intracellular
255 density in which the ends that were actively growing appeared less dense than the non-growing
256 ends (Figure 6A). We hypothesized that these subcellular gradients reflected differences in tip
257 growth between the two ends of the cell. In agreement with our hypothesis, the slower-growing
258 new end typically appeared denser than the faster-growing end (Figure 6A). In some cells, the
259 difference in densities between the fast- and slow-growing ends was ~10% of the mean overall
260 density (Figure 6A). The mean density difference between the two ends throughout the cell cycle
261 was ~15 mg/mL, corresponding to ~5% of the mean overall density (Figure 6B). To address the
262 potential for differences in the widths (and hence heights above the coverslip) of old and new

263 ends to influence phase shifts (Figure S6A), we constrained our analysis to cells within a narrow
264 range of widths and found that local density and tip growth remained highly correlated (Figure
265 S6B). Examples of post-cytokinesis cells with adjacent compartments exhibiting different
266 densities (see Figures 7, S7 below) further indicated that these differences could not be
267 explained simply by width differences. Since tip growth is regulated by actin-dependent
268 mechanisms (32-34), we tested whether maintenance of the gradient is dependent on F-actin or
269 tip growth: we found that in cells treated with latrunculin A, spatial density gradients persisted
270 over time (Figure S6C). These results demonstrate that intracellular density gradients are stable
271 and linked to local growth patterns, and that their maintenance does not require active growth
272 or F-actin.
273
274 We noticed asymmetries in density between daughter cells after cell division, in which one of the
275 daughters was denser than its sister. Time-lapse imaging showed that the intracellular density
276 differences established during interphase were often propagated through cell division and
277 correlated with density differences between the progeny daughter cells after cytokinesis (Figure
278 6D,E). Thus, subcellular density variations are stable enough to be propagated through
279 generations.
280
281 **Cell density differences are linked to intracellular osmotic pressure**
282 Next, we ascertained whether density variations of 5-20% – the magnitude observed within and
283 across cells with normal physiology – have physiological consequences. One variable potentially
284 connected with intracellular density is macromolecular crowding. High concentrations of
285 macromolecules are predicted to produce colloid osmotic pressure that may influence cell
286 mechanics (2). As noted above, the densities of daughter compartments in septated cells were

287 often different from each other (Figure 6D,E); these differences were often exacerbated in cells
288 with cell-division defects, such as *mid1*, *mid2*, and *cdc16* cells. We noted that the septum between
289 these daughter cells generally bent away from the more dense compartment (Figure S7).
290 Previous studies (22) reported that the septum is an elastic structure that can be used as a
291 biosensor that reports on osmotic pressure differences between compartments. For instance,
292 when one daughter is lysed by laser microsurgery and loses turgor pressure, the septum bulges
293 away from the intact daughter (22). Temporal fluctuations in septum bending have been
294 proposed to arise from fluctuations in pressure differences between daughter cells (35).
295
296 To investigate the relationship between density differences and septum bending, we focused on
297 *mid2Δ* cells. Mid2 is an anillin ortholog that regulates septins in late cytokinesis; *mid2Δ* mutants
298 exhibit long delays (1-2 h) in cell separation and thus most cells in the population have one or
299 more septa (36). We used QPI to track intracellular density over time and identified the time
300 after septum formation at which the maximum density difference was reached for each cell. Of
301 the 71% (64/90) of cells exhibiting a bent septum, 97% (62/64) exhibited a septum bent away
302 from the compartment of higher density at the time of maximum density difference (Figure 7A),
303 with a mean maximum difference of 16±5% (Figure 7B). In 2/90 cells, the septum was bent in
304 the opposite manner, toward the compartment of lower density; in these rare instances, the
305 maximum density difference was substantially lower (5%; Figure 7B) and may represent cases in
306 which the septum is fluctuating in direction. Indeed, in one cell the fluctuating direction of
307 septum bending coincided with alternation of the sign of the density difference between the
308 daughter cells (Figure 7C). In instances where the septum appeared flat, the density difference
309 was substantially lower (~4.5%) than in cells with a bent septum.
310

311 We also noted density variations and bent septa in multi-septated *mid2Δ* cells. In particular,
312 internal compartments bounded by two septa were hampered in their ability to grow in volume
313 and correspondingly exhibited higher density than the surrounding compartments (Figure 7D)
314 These situations were frequently associated with both septa bending away from the higher-
315 density compartment (Figure 7D). The observation that septal bending occurred for density
316 differences as low as 5-10% suggests that the density variations over the course of a normal cell
317 cycle (Figure 2), in cell cycle arrested cells (Figure 3, 4, 5) or between growing and non-growing
318 cell tips (Figure 6) may reflect substantial changes in turgor-mediated stresses.

319 **Discussion**

320 Here, we established a QPI method based on *z*-stacks of brightfield images for quantifying
321 intracellular density dynamics in living cells. We found that exponential-phase fission yeast cells
322 have a dry-mass density of 282±16 mg/mL (Figure 1C-E) and a buoyant-mass density of
323 1.108±0.005 g/mL (Figure 2D), comparable to measurements in other organisms (3, 37). Density
324 varied systematically across the cell cycle in wild-type fission yeast cells over a range of ~10%
325 (Figure 2C), while the relative rate of dry-mass synthesis remained constant (reflecting
326 exponential accumulation) throughout all cell-cycle stages (Figure 2F,G). These quantitative
327 findings, which utilize precise sub-pixel measurements of cellular dimensions and automated
328 analysis platforms, are consistent with more qualitative density studies of fission yeast using
329 other methods (17, 38, 39).

330

331 Our data support a model in which these density variations during the cell cycle are a product of
332 programmed changes in volume growth accompanied by a constant relative rate of mass
333 biosynthesis. Accordingly, volume growth and biosynthesis were not tightly coupled throughout
334 the cell cycle. During tip growth in G2 phase, intracellular density dropped steadily (Figure 2C,
335 3C), indicating that the rate of volume growth outpaces biosynthesis during this period. Density
336 steadily rose during mitosis and cytokinesis (Figure 2C), when volume growth ceases or slows.
337 After separation of daughter cells (cell birth), density dropped during the rapid increase in cell
338 volume as the new cell end expanded (Figure 2E), possibly due to water influx. Despite these
339 changes in growth rate and density, it is remarkable that even without tight feedback controls,
340 cells maintained a relatively tight distribution (CV~6%) of densities across the population
341 (Figure 1C).

342

343 Consistent with this model, density shifts were exacerbated by perturbations of cell-cycle
344 progression or of volume growth directly. *cdc25* mutants delayed in G2 phase exhibited a steady
345 decline in density as cells elongated abnormally (Figure 3), reminiscent of the cytoplasmic
346 dilution observed in very enlarged budding yeast cells and senescent mammalian cells (9).
347 During mitotic arrest at the spindle checkpoint (*cut7*) or cytokinesis arrest through regulation of
348 the SIN pathway (*cdc16*), volume growth was slowed but mass synthesis was unaffected,
349 resulting in steady density increases (Figure 4C,E). Inhibition of cell growth with latrunculin A
350 caused a steady increase in density regardless of cell cycle stage (Figure 5). These findings
351 suggest that any perturbation that affects cell-cycle progression or growth is likely to alter
352 density dynamics. Cell-cycle arrests are commonly used to synchronize cells and are often
353 triggered in response to stresses such as DNA damage. Our study demonstrates that such
354 perturbations are not as innocuous as often thought; arrests not only affect cell-cycle
355 progression and cell size, but also cause changes in intracellular density and potentially other
356 downstream changes in physiology.
357
358 Our studies provide quantitative measurements of the mass dynamics of individual fission yeast
359 cells throughout the cell cycle. We found that mass accumulation was continuous, consistent with
360 previous studies (38, 39). Notably, our quantitative measurements suggested that mass
361 dynamics were exponential in nature (Figure 2F,G, S2F), consistent with findings in other cell
362 types (40). Intriguingly, studies of density and growth in other cell types reported somewhat
363 different cell-cycle patterns. In budding yeast, buoyant density is lowest in early G1 and rises in
364 late G1 and S phase at the time of bud formation (37). Moreover, cell-cycle arrests in S and M
365 phase and latrunculin A treatment do not lead to increases in buoyant density in budding yeast,
366 unlike our findings in fission yeast (Figure 5). In human cells, mass growth continues in early

367 mitosis, but stops in metaphase and resumes in late cytokinesis, potentially with subtle
368 oscillations (41, 42). Density is constant in human cells during much of the cell cycle, but
369 decreases in mitosis (by 0.5% in buoyant mass, equivalent to >10% decrease in dry-mass
370 density) coincident with a 10-30% volume increase during mitotic rounding; density then
371 slightly increases in cytokinesis (6, 7). In the bacterium *Escherichia coli*, density varies somewhat
372 from birth to division, but the ratio of surface area to mass is relatively constant, suggesting that
373 biosynthesis is linked to surface-area synthesis (43). Here we found that in fission yeast, mass
374 was also more closely coupled with surface area than volume, especially when the surface area of
375 both sides of the septum were factored in (Figure S4B-D). However, examples such as latruculin
376 A-treated cells (Figure 5B) demonstrated that mass accumulation and surface area growth are
377 not inextricably linked and can be uncoupled. It remains to be seen whether general rules of cell-
378 density regulation will emerge from comparisons across organisms and cell types.
379
380 Our findings also provide insight into the relationship between the rate of volume growth and
381 subcellular density regulation. Fission yeast cells grow through tip growth, which involves the
382 extension and assembly of new cell wall and plasma membrane at the growing tip; this growth is
383 accomplished by a complex integration of the cell-polarity machinery, exocytosis, wall growth
384 and mechanics, and turgor pressure (25, 34). In addition to the global effect of volume growth on
385 density, the intriguing polarization of density patterns that we discovered (Figure 6) suggests
386 that tip growth influences local intracellular density patterns more directly. Spatial gradients
387 revealed that local density was correlated with tip growth, with growing ends having lower
388 density (Figure 6C). It is not yet clear what cellular components are responsible for this spatial
389 pattern, and whether they are actively depleted at growing cell tips or concentrated at non-
390 growing regions. The relevant components may be membrane-bound or membrane-less

391 organelles; it is unlikely that they are soluble, freely diffusing particles, unless a diffusion barrier
392 (perhaps the nucleus) exists. The distributions of large organelles and total protein are not
393 polarized in this manner (44, 45) . However, polarized patterns have been detected in
394 immunofluorescence of damaged (carbonylated) proteins, which may impact replicative aging
395 (46). Polarized density patterns established in interphase were often propagated through cell
396 division and appeared to be inherited by the daughter cells, resulting in differences in density
397 across a lineage (Figure 6D,E). How these patterns may lead to asymmetric behaviors in cell
398 lineages such as growth patterns and aging remains to be explored (34, 46). Spatial
399 heterogeneities in density have also been observed in mammalian cells; it remains to be
400 determined whether these patterns are related to cell shape, organelles, or variations in
401 cytoplasmic density (5, 47, 48).
402
403 The effects of changes in intracellular density on cellular functions are only beginning to be
404 appreciated. The density changes of 5-20% that we observed, which likely affect the
405 concentration of most if not all cellular components in the cytoplasm, could have profound
406 consequences for the biochemistry of cellular reactions and on macromolecular crowding. Here
407 we provided evidence that density may also affect cell mechanics and thereby influence cell
408 shape. Intracellular osmotic pressure and density differences between daughter compartments
409 were strongly coupled, as evidenced by bending of the elastic septal cell wall (Figure 7). Density
410 may affect pressure through effects on macromolecular crowding, which produces colloid
411 osmotic pressure associated with the displacement of water (2). Differences in colloid osmotic
412 pressure have been proposed to influence nuclear size (2, 49), but experimental evidence linking
413 crowding to force generation *in vivo* generally remains scant. Our findings thus lend important
414 support to the idea that different densities of macromolecules can generate large enough

415 differences in colloid osmotic pressure to alter cell shape. We speculate that the increase of
416 density at cell division may provide mechanical force through increased turgor pressure to
417 facilitate cell-cell separation and bulging of the cell wall (22), and may affect the distribution of
418 mechanical stresses within the cell wall during other cell-cycle stages as well.
419
420 Another possible consequence of intracellular density changes is the regulation of volume
421 growth rate. In fission yeast, perturbations that increase density are followed by a dramatic
422 increase in volume growth rate that persists for hours (10). How density impacts volume growth
423 rate, possibly via the concentration of certain intracellular factors or through effects on
424 intracellular pressure, remains to be elucidated. Thus, toggling the rate of volume growth may
425 play an important role in density homeostasis. Future studies focusing on the effects of cell
426 density on particular cellular processes will be needed to understand the full scope of
427 consequences of density variations on cell physiology.

428 **Methods**

429

430 **Strains and cell culturing**

431 All strains used in this study are listed in Table S1. Methods for propagation and growth of *S.*
432 *pombe* cells were as described in (50). In general, cultures were grown in 3 mL of YE5S medium
433 at 30 °C on a rotating shaker overnight to OD_{600}~1, diluted to OD_{600}~0.1, and incubated until
434 OD_{600}~0.3 for imaging. Temperature sensitive mutant c*dc25-22* cells (and wild-type control
435 cells) were first grown at room temperature; 90 min after imaging started, the temperature was
436 increased to 32 °C. Temperature-sensitive mutant *cdc16-116* cells (and wild-type control cells)
437 were first grown at 25 °C, then imaged on the microscope with the temperature-controlled
438 enclosure pre-heated to 34 °C. Temperature-sensitive mutant *cut7-446* cells (and wild-type
439 control cells) were first grown at 25 °C, then imaged on the microscope with the temperature-
440 controlled enclosure pre-heated to 30 °C.

441

442 **Single-cell imaging**

443 Images were acquired with a Ti-Eclipse inverted microscope (Nikon) equipped with a 680-nm
444 bandpass filter (D680/30, Chroma Technology) in the illumination path with a 60X (NA: 1.4) DIC
445 oil objective (Nikon). Before imaging, Koehler illumination was configured and the peak
446 illumination intensity at 10-ms exposure time was set to the middle of the dynamic range of the
447 Zyla sCMOS 4.2 camera (Andor Technology). μManager v. 1.41 (51) was used to automate
448 acquisition of *z*-stack brightfield images with a step size of 250 nm from ±3 μm around the focal
449 plane (total of 25 imaging planes) to ensure substantial oversampling that facilitated correcting
450 for potential drift in the *z*-direction over the course of each experiment at 5- or 10-min intervals
451 at multiple (*x,y*) positions.

452

453 **Microfluidics**

454 Cellasic microfluidic flow cell plates (Millipore, Y04C) controlled by an ONIX or ONIX2
455 (Millipore) microfluidic pump system were used for imaging. YE5S medium was loaded into all
456 but one of the fluid reservoirs; the remaining well was loaded with 100 mg/mL bovine serum
457 albumin (BSA) (Sigma Aldrich) in YE5S. Liquid was flowed from all 6 channels for at least 5 min
458 at 5 psi (corresponding to 34.5 kPa), followed by 5 min of flow from YE5S-containing wells to
459 wash out buffer and to fill channels and imaging chambers. The plate was kept in a temperature-
460 controlled enclosure (OkoLab) throughout loading. Cells were then transferred into the
461 appropriate well and loaded into the microfluidic imaging chamber such that a small number of
462 cells were initially trapped, and flow of YE5S was applied. To ensure full exchange of liquid in the
463 chamber during imaging, the flow channel was switched at least 40 s before images were
464 acquired. Every ~2 h, BSA flow was activated during one time point of imaging to calibrate QPI
465 measurements.

466

467 **Image analysis to retrieve phase shifts**

468 To reduce post-processing time, each *z*-stack was cropped to a square region containing the
469 cell(s) of interest and a border of at least 40 pixels, and the focal plane was identified. This
470 cropping was accomplished first using FIJI v. 1.53c to identify regions of interest (ROIs) within a
471 thresholded standard deviation *z*-projection image of each brightfield *z*-stack. Using custom
472 Matlab R2019a (Mathworks) scripts, images were cropped to the ROIs and the standard
473 deviation of the pixels in each ROI was computed. The focal plane was defined based on the
474 image in the stack with the lowest standard deviation. Three images above and three images
475 below the focal plane separated by 500 nm were used to quantify cytoplasmic density. Based on

476 these images, the phase information was calculated using a custom Matlab script implementing a
477 previously published algorithm (15). In brief, this method relates the phase information of the
478 cell to brightfield image intensity changes along the *z*-direction. Equidistant, out-of-focus images
479 above and below the focal plane are used to estimate intensity changes at various defocus
480 distances. A phase-shift map is reconstructed in a non-linear, iterative fashion to solve the
481 transport-of-intensity equation.
482
483 **Cytoplasmic density quantification**
484 Using Matlab, images were background-corrected by fitting a Gaussian to the highest peak of the
485 histogram (corresponding to the background pixels) of the phase-shift map and shifting every
486 pixel so that the background intensity peak corresponded to zero phase shift. These background-
487 corrected phase-shift maps were converted into binary images using watershedding for cell
488 segmentation; where necessary, binary images were corrected manually to ensure accurate
489 segmentation. Binary images were segmented using Morphometrics (52) to generate subpixel-
490 resolved cell outlines.
491
492 Each cell outline was skeletonized using custom Matlab code as follows. First, the closest-fitting
493 rectangle around each cell was used to define the long axis of the cell. Perpendicular to the long
494 axis, sectioning lines at 250-nm intervals and their intersection with the cell contour were
495 computed. The centerline was then updated to run through the midpoint of each sectioning line
496 between the two contour-intersection points. The slope of each sectioning line was updated to be
497 perpendicular to the slope of the centerline around the midpoint. Sectioning lines that crossed a
498 neighboring line were removed. Cell volume and surface area were calculated by summing the

499 volume or area of each section, assuming rotational symmetry. Volume and area of the poles
500 were calculated assuming a regular spherical cap.
501
502 To convert the mean intensity of the phase-shift within each cell into absolute concentration (in
503 units of mg/mL), the mean of all cells across all time points was first calculated. Then, the
504 decrease in phase shift induced by a prescribed concentration of BSA (typically 100 mg/mL) was
505 defined as the difference between the mean of the phase shifts before and after the BSA imaging
506 time point and the phase shift during the BSA time point. This difference in intensity established
507 the calibration scaling between phase shift intensity and the concentration of BSA (Figure 1B).
508 The cytoplasmic density of each cell was then calculated by dividing the mean phase shift of the
509 cell by the aforementioned scaling factor. The mass of each cell was inferred from its mean
510 density and volume.
511
512 **BSA calibration**
513 Channel slides (μ-Slide VI 0.4, ibidi) were treated with lectin (Sigma-Aldrich, L1395) (0.1 mg/mL
514 in water) for ~5 min, washed with YE5S, and cells were added and incubated for ~5 min to allow
515 for attachment. Unattached cells were removed by washing with YE5S. Attached cells were first
516 imaged in YE5S medium. Freshly prepared BSA (Sigma-Aldrich, A3608) was then added to a final
517 concentration of 200 mg/mL. YE5S was added to dilute BSA to the desired concentrations (150,
518 100, and 50 mg/mL), followed by washout of the BSA and imaging in YE5S.
519
520 **Lipid droplet staining**
521 Lipid droplets were stained with the dye BODIPY 493/503 (Thermo Fisher, D3922) (53).
522 Aliquots (10 μL) of 100 mM BODIPY in absolute ethanol were prepared. Ethanol was then

523 evaporated in a desiccator under vacuum and dried aliquots were stored at 4 °C for long-term
524 storage. For use, an aliquot was redissolved in 10 μL absolute ethanol and 1 μL was added to 1
525 mL of cell culture in YE5S for each unit of cell density with OD_{600}=0.1 and incubated protected
526 from light for ~1 min at room temperature. Cells were then pelleted at 0.4 rcf in a microfuge for
527 1 min and medium was exchanged with fresh YE5S. Cells were spotted onto agarose pads and
528 imaged with an EM-CCD camera (Hamamatsu) through a spinning-disk confocal system
529 (Yokogawa CSU-10) attached to one of the ports of a Ti-Eclipse inverted microscope with a 488-
530 nm laser. In parallel, brightfield *z*-stack images were acquired for QPI.
531

532 **Lineage tracking for time-lapse imaging datasets**

533 First, each cell present at the beginning of the experiment was linked to the closest cell in the
534 next frame based on the distance between centers and the difference in their size (cross-
535 sectional area). A cell was considered the same if the centers between consecutive time points
536 were within 20 pixels (~2 μm) and the cross-sectional area was >70% of the area at the previous
537 time point. This process was iterated to define the lineage until either requirement was violated
538 (usually due to cell division), at which point a new lineage was initialized using the earliest
539 unassigned cell. All lineages were visually inspected and corrected when necessary.
540

541 **Polar growth and density quantification**

542 To separately quantify the growth of the new and old ends, fiduciary markers such as birth scars
543 on the cell outline were identified from which the distance to each pole at the beginning and
544 completion of the cell cycle was measured. The density of each polar region was calculated by
545 extracting the peak of the histogram of density values in the region within 3 μm of the pole at
546 each time point, and then calculating the mean over time points.

547

548 **Suspended microchannel resonator (SMR) measurements**

549 SMR-based density and volume measurements were carried out according to a previously
550 reported fluid-switching method (18). Briefly, the SMR measures the buoyant mass of a cell by
551 flowing in culture medium through a vibrating cantilever and measuring changes in vibration
552 frequency. The cell is then mixed with a denser medium composed of 50% culture medium and
553 50% OptiPrep (Sigma-Aldrich), and flowed back through the cantilever to obtain a second
554 buoyant mass measurement 10 s later. Cell volume and density are calculated from the two
555 consecutive buoyant mass measurements based on the known densities of the two fluids (18).
556 Each cell is serially flushed into the system in culture medium from a reservoir at 30 °C. After
557 every hour of measurement, the reservoir is replenished from an exponential-phase culture.

558

559 SMR devices were fabricated at CEA-LETI (Grenoble, France). The physical dimensions and
560 operation of the SMR, as well as data analyses, were identical to those reported in (42, 54).
561 Briefly, the SMR cantilever was vibrated in the second flexural bending mode using a piezo-
562 ceramic plate underneath the SMR chip. The vibration frequency of the cantilever was measured
563 using piezo-resistors at the base of the cantilever. A digital control platform was used to drive
564 the cantilever in a feedback mode, where the vibration frequency signal acquired from the piezo-
565 resistor was delayed, amplified, and used as the drive signal to actuate the cantilever. Fluid flow
566 was controlled using two electronic pressure regulators and solenoid valves, which were used to
567 pressurize vials containing the culture medium. A typical cell transit time through the cantilever
568 was 150 ms. System temperature was controlled by mounting the SMR and culture-medium vials
569 on copper stands connected to a heated water bath. All SMR operations were controlled using
570 National Instruments control cards and custom LabVIEW (2012) code. Frequency data were

571 analyzed using previously reported custom Matlab code that measures the maximum frequency
572 change during the transit of each cell through the cantilever (54). Frequency measurements
573 were calibrated using polystyrene beads and NaCl solutions of known density.
574

575 **Holographic refractive index measurements**

576 For refractive index measurements, wild-type *S. pombe* cells grown at 30 °C were immobilized on
577 a lectin-coated glass-bottom 35 mm diameter μ-dish (ibidi). Holographic refractive index
578 measurements were acquired with a 3D Cell Explorer system (Nanolive) with a temperature-
579 controlled enclosure set to 30 °C. First, sum images of *z*-stacks of three-dimensional refractive
580 index maps were generated to retrieve cell outlines by watershedding. Cells oriented at an angle
581 to the flat glass bottom dish were ignored. For each remaining cell, the mean refractive index was
582 extracted from each image in the *z*-stack using Matlab and the highest value (assumed to
583 correspond to the middle plane) was used for further analysis.
584

585 **Lipid droplet staining**

586 Lipid droplets were stained with the dye BODIPY 493/503 (Thermo Fisher, D3922) (53).
587 Aliquots (10 μL) of 100 mM BODIPY in absolute ethanol were prepared. Ethanol was then
588 evaporated in a desiccator under vacuum and dried aliquots were stored at 4 °C for long-term
589 storage. For use, an aliquot was redissolved in 10 μL absolute ethanol and 1 μL was added to 1
590 mL of cell culture in YE5S for each unit of cell density with OD_{600}=0.1 and incubated protected
591 from light for ~1 min at room temperature. Cells were then pelleted at 0.4 rcf in a microfuge for
592 1 min and medium was exchanged with fresh YE5S. Cells were spotted onto agarose pads and
593 imaged with an EM-CCD camera (Hamamatsu) through a spinning-disk confocal system

594 (Yokogawa CSU-10) attached to one of the ports of a Ti-Eclipse inverted microscope with a 488-
595 nm laser. In parallel, brightfield *z*-stack images were acquired for QPI.
596
597 **Latrunculin A treatment**
598 Stock solutions were made by dissolving 100 μg latrunculin A (Abacam, ab144290) in dimethyl
599 sulfoxide (DMSO, Sigma-Aldrich) to a concentration of 20 mM and stored at -20 °C in 1-μL
600 aliquots. To prepare agarose pads, 1 μL of 20 mM latrunculin A or 1 μL of DMSO was mixed with
601 100 μL of YE5S medium containing 2% (w/v) agarose UltraPure agarose (Invitrogen
602 Corporation) kept in a water bath at ~70 °C. The mixture was pipetted onto a microscope glass
603 slide and quickly covered with another slide to form flat agarose pads with thickness of ~2 mm.
604 Once pads had solidified, one slide was carefully removed and 1-2 μL of exponential-phase wild-
605 type cells were deposited on the agarose pad. Cells were allowed to settle for 1-2 min before a
606 coverslip was placed on top and sides were sealed with Valap (1:1:1 vaseline:lanolin:paraffin) to
607 prevent evaporation during imaging.
608
609 **Statistical analyses**
610 The magnitude of the correlation between two continuous variables was reported using
611 Pearson's correlation coefficient. R^2 and associated *p*-values were calculated using the built-in
612 function corrcoef in Matlab R2019a (Mathworks).

613 **Acknowledgments**

614 We thank the Chang and Huang labs for discussion and support, Gabriella Estevam for her
615 contributions to the project at its early stages, Scott M. Knudsen for assisting with cell culturing
616 for SMR measurements, and Sophie Dumont and her lab for discussion. P.D.O. was supported by
617 postdoctoral fellowships from the Swiss National Science Foundation under Grants
618 P2ELP3_172318 & P400PB_180872. F.C. was supported by NIH GM056836. T.P.M. received
619 funding from the Wellcome Trust (110275/Z/15/Z). K.C.H. is a Chan Zuckerberg Biohub
620 investigator.

621 **References**

622

623 1. J. van den Berg, A. J. Boersma, B. Poolman, Microorganisms maintain crowding
624 homeostasis. *Nat Rev Microbiol* **15**, 309-318 (2017).
625 2. T. J. Mitchison, Colloid osmotic parameterization and measurement of subcellular
626 crowding. *Mol Biol Cell* **30**, 173-180 (2019).
627 3. G. E. Neurohr, A. Amon, Relevance and Regulation of Cell Density. *Trends Cell Biol* **30**, 213-
628 225 (2020).
629 4. H. X. Zhou, G. Rivas, A. P. Minton, Macromolecular crowding and confinement:
630 biochemical, biophysical, and potential physiological consequences. *Annu Rev Biophys* **37**,
631 375-397 (2008).
632 5. S. Oh *et al.*, In situ measurement of absolute concentrations by Normalized Raman
633 Imaging. *bioRxiv* 10.1101/629543, 629543 (2019).
634 6. S. Son *et al.*, Resonant microchannel volume and mass measurements show that
635 suspended cells swell during mitosis. *J Cell Biol* **211**, 757-763 (2015).
636 7. E. Zlotek-Zlotkiewicz, S. Monnier, G. Cappello, M. Le Berre, M. Piel, Optical volume and
637 mass measurements show that mammalian cells swell during mitosis. *J Cell Biol* **211**, 765-
638 774 (2015).
639 8. E. R. Rojas, K. C. Huang, Regulation of microbial growth by turgor pressure. *Curr Opin*
640 *Microbiol* **42**, 62-70 (2018).
641 9. G. E. Neurohr *et al.*, Excessive Cell Growth Causes Cytoplasm Dilution And Contributes to
642 Senescence. *Cell* **176**, 1083-1097.e1018 (2019).
643 10. B. D. Knapp *et al.*, Decoupling of Rates of Protein Synthesis from Cell Expansion Leads to
644 Supergrowth. *Cell Syst* **9**, 434-445.e436 (2019).

645 11. T. A. Zangle, M. A. Teitell, Live-cell mass profiling: an emerging approach in quantitative
646 biophysics. *Nat Methods* **11**, 1221-1228 (2014).
647 12. T. P. Burg *et al.*, Weighing of biomolecules, single cells and single nanoparticles in fluid.
648 *Nature* **446**, 1066-1069 (2007).
649 13. Y. Park, C. Depeursinge, G. Popescu, Quantitative phase imaging in biomedicine. *Nature*
650 *Photonics* **12**, 578-589 (2018).
651 14. K. Lee *et al.*, Quantitative phase imaging techniques for the study of cell pathophysiology:
652 from principles to applications. *Sensors (Basel, Switzerland)* **13**, 4170-4191 (2013).
653 15. E. Bostan, E. Froustey, M. Nilchian, D. Sage, M. Unser, Variational Phase Imaging Using the
654 Transport-of-Intensity Equation. *IEEE Trans Image Process* **25**, 807-817 (2016).
655 16. J. M. Mitchison, P. Nurse, Growth in cell length in the fission yeast Schizosaccharomyces
656 pombe. *J Cell Sci* **75**, 357-376 (1985).
657 17. B. Rappaz *et al.*, Noninvasive characterization of the fission yeast cell cycle by monitoring
658 dry mass with digital holographic microscopy. *J Biomed Opt* **14**, 034049 (2009).
659 18. W. H. Grover *et al.*, Measuring single-cell density. *Proc Natl Acad Sci U S A* **108**, 10992-
660 10996 (2011).
661 19. F. Feijó Delgado *et al.*, Intracellular water exchange for measuring the dry mass, water
662 mass and changes in chemical composition of living cells. *PloS one* **8**, e67590-e67590
663 (2013).
664 20. A. B. Martín-Cuadrado, E. Dueñas, M. Sipiczki, C. R. Vázquez de Aldana, F. del Rey, The
665 endo-beta-1,3-glucanase eng1p is required for dissolution of the primary septum during
666 cell separation in Schizosaccharomyces pombe. *J Cell Sci* **116**, 1689-1698 (2003).

667 21. B. S. Hercyk, U. N. Onwubiko, M. E. Das, Coordinating septum formation and the
668 actomyosin ring during cytokinesis in Schizosaccharomyces pombe. *Mol Microbiol* **112**,
669 1645-1657 (2019).
670 22. E. Atilgan, V. Magidson, A. Khodjakov, F. Chang, Morphogenesis of the Fission Yeast Cell
671 through Cell Wall Expansion. *Curr Biol* **25**, 2150-2157 (2015).
672 23. V. Simanis, Pombe's thirteen – control of fission yeast cell division by the septation
673 initiation network. *Journal of Cell Science* **128**, 1465 (2015).
674 24. S. Ray *et al.*, The mitosis-to-interphase transition is coordinated by cross talk between the
675 SIN and MOR pathways in Schizosaccharomyces pombe. *Journal of Cell Biology* **190**, 793-
676 805 (2010).
677 25. S. G. Martin, R. A. Arkowitz, Cell polarization in budding and fission yeasts. *FEMS*
678 *Microbiology Reviews* **38**, 228-253 (2014).
679 26. A. Papagiannakis, B. Niebel, E. C. Wit, M. Heinemann, Autonomous Metabolic Oscillations
680 Robustly Gate the Early and Late Cell Cycle. *Mol Cell* **65**, 285-295 (2017).
681 27. B. Novak, J. M. Mitchison, Change in the rate of CO2 production in synchronous cultures of
682 the fission yeast Schizosaccharomyces pombe: a periodic cell cycle event that persists
683 after the DNA-division cycle has been blocked. *J Cell Sci* **86**, 191-206 (1986).
684 28. J. M. Mitchison, "Growth During the Cell Cycle" in International Review of Cytology.
685 (Academic Press, 2003), vol. 226, pp. 165-258.
686 29. P. Nurse, P. Thuriaux, K. Nasmyth, Genetic control of the cell division cycle in the fission
687 yeast Schizosaccharomyces pombe. *Molecular and General Genetics MGG* **146**, 167-178
688 (1976).
689 30. I. Hagan, M. Yanagida, Novel potential mitotic motor protein encoded by the fission yeast
690 cut7+ gene. *Nature* **347**, 563-566 (1990).

691 31. M. Minet, P. Nurse, P. Thuriaux, J. M. Mitchison, Uncontrolled septation in a cell division
692 cycle mutant of the fission yeast Schizosaccharomyces pombe. *J Bacteriol* **137**, 440-446
693 (1979).
694 32. K. Z. Pan, T. E. Saunders, I. Flor-Parra, M. Howard, F. Chang, Cortical regulation of cell size
695 by a sizer cdr2p. *eLife* **3**, e02040 (2014).
696 33. D. R. Mutavchiev, M. Leda, K. E. Sawin, Remodeling of the Fission Yeast Cdc42 Cell-Polarity
697 Module via the Sty1 p38 Stress-Activated Protein Kinase Pathway. *Current biology : CB* **26**,
698 2921-2928 (2016).
699 34. F. Chang, S. G. Martin, Shaping fission yeast with microtubules. *Cold Spring Harb Perspect*
700 *Biol* **1**, a001347 (2009).
701 35. J. Muñoz *et al.*, Extracellular cell wall β(1,3)glucan is required to couple septation to
702 actomyosin ring contraction. *The Journal of cell biology* **203**, 265-282 (2013).
703 36. A. Berlin, A. Paoletti, F. Chang, Mid2p stabilizes septin rings during cytokinesis in fission
704 yeast. *J Cell Biol* **160**, 1083-1092 (2003).
705 37. A. K. Bryan, A. Goranov, A. Amon, S. R. Manalis, Measurement of mass, density, and volume
706 during the cell cycle of yeast. *Proc Natl Acad Sci U S A* **107**, 999-1004 (2010).
707 38. J. M. Mitchison, The growth of single cells. I. Schizosaccharomyces pombe. *Exp Cell Res* **13**,
708 244-262 (1957).
709 39. V. Stonyte, E. Boye, B. Grallert, Regulation of global translation during the cell cycle. *J Cell*
710 *Sci* **131** (2018).
711 40. M. Godin *et al.*, Using buoyant mass to measure the growth of single cells. *Nat Methods* **7**,
712 387-390 (2010).

713 41. X. Liu, S. Oh, L. Peshkin, M. W. Kirschner, Computationally Enhanced Quantitative Phase
714 Microscopy Reveals Autonomous Oscillations in Mammalian Cell Growth. *bioRxiv*
715 10.1101/631119, 631119 (2019).
716 42. T. P. Miettinen, J. H. Kang, L. F. Yang, S. R. Manalis, Mammalian cell growth dynamics in
717 mitosis. *Elife* **8** (2019).
718 43. E. R. Oldewurtel, Y. Kitahara, B. Cordier, G. Özbaykal, S. van Teeffelen, Bacteria control cell
719 volume by coupling cell-surface expansion to dry-mass growth. *bioRxiv* 10.1101/769786,
720 769786 (2019).
721 44. D. Y. Parkinson, G. McDermott, L. D. Etkin, M. A. Le Gros, C. A. Larabell, Quantitative 3-D
722 imaging of eukaryotic cells using soft X-ray tomography. *J Struct Biol* **162**, 380-386
723 (2008).
724 45. K. Kume *et al.*, A systematic genomic screen implicates nucleocytoplasmic transport and
725 membrane growth in nuclear size control. *PLoS Genet* **13**, e1006767 (2017).
726 46. N. Erjavec, M. Cvijovic, E. Klipp, T. Nyström, Selective benefits of damage partitioning in
727 unicellular systems and its effects on aging. *Proc Natl Acad Sci U S A* **105**, 18764-18769
728 (2008).
729 47. W. Choi *et al.*, Tomographic phase microscopy. *Nat Methods* **4**, 717-719 (2007).
730 48. O. Tolde *et al.*, Quantitative phase imaging unravels new insight into dynamics of
731 mesenchymal and amoeboid cancer cell invasion. *Sci Rep* **8**, 12020 (2018).
732 49. C. V. Harding, C. Feldherr, Semipermeability of the nuclear membrane in the intact cell. *J*
733 *Gen Physiol* **42**, 1155-1165 (1959).
734 50. S. Moreno, A. Klar, P. Nurse, Molecular genetic analysis of fission yeast
735 Schizosaccharomyces pombe. *Methods Enzymol* **194**, 795-823 (1991).

736 51. A. D. Edelstein *et al.*, Advanced methods of microscope control using μManager software. *J*
737 *Biol Methods* **1** (2014).
738 52. T. Ursell *et al.*, Rapid, precise quantification of bacterial cellular dimensions across a
739 genomic-scale knockout library. *BMC Biol* **15**, 17 (2017).
740 53. A. Meyers *et al.*, Lipid Droplets Form from Distinct Regions of the Cell in the Fission Yeast
741 Schizosaccharomyces pombe. *Traffic* **17**, 657-669 (2016).
742 54. J. H. Kang *et al.*, Noninvasive monitoring of single-cell mechanics by acoustic scattering.
743 *Nat Methods* **16**, 263-269 (2019).
744

Figures

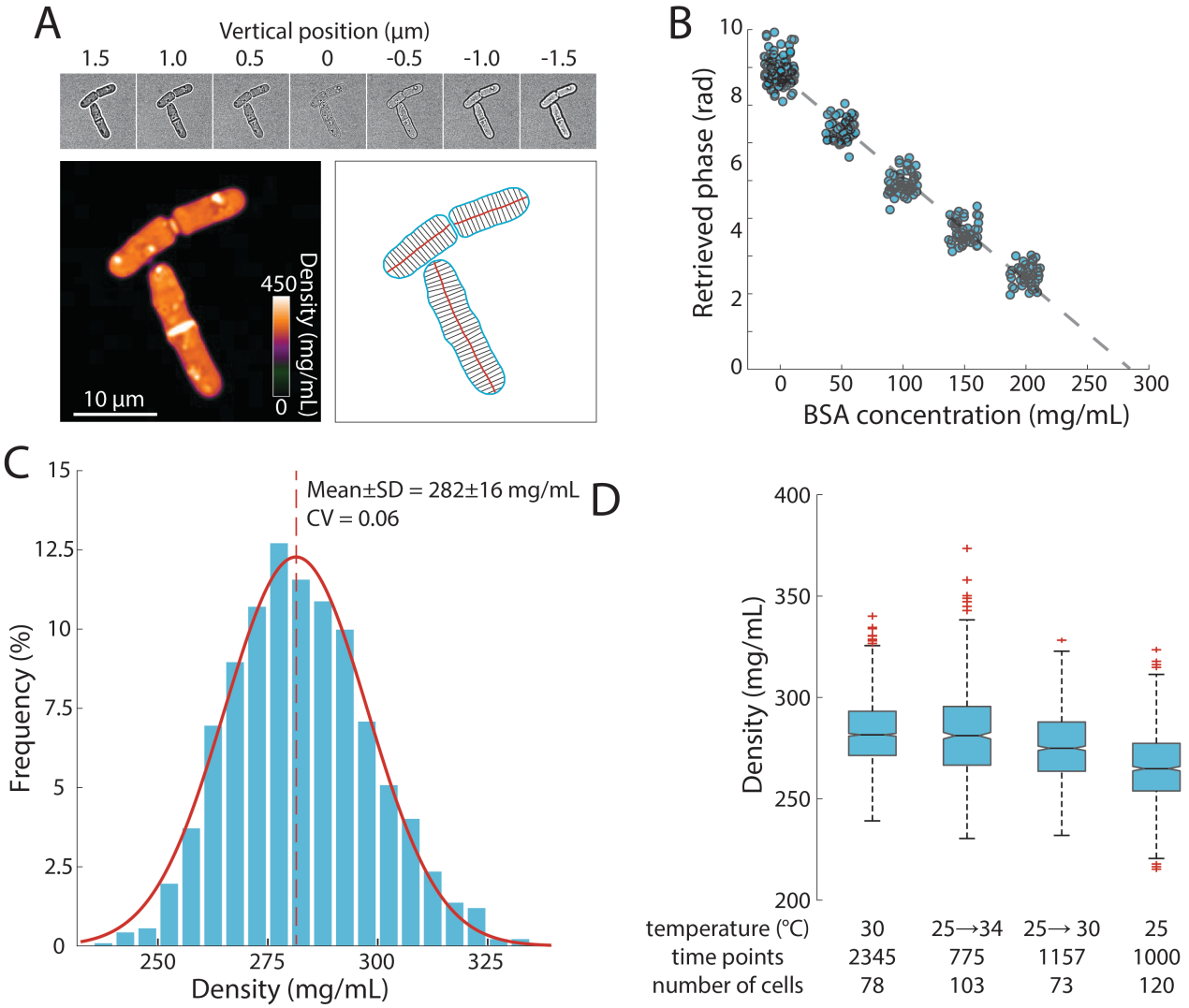

Figure 1: Precise measurement of intracellular density using QPI based on a *z*-stack of brightfield images.

A) QPI method for computing cytoplasmic density from brightfield images. A *z*-stack of brightfield images of fission yeast cells ±1.5 μm around the focal position (top) were computationally analyzed by solving the transport-of-intensity equation (15) to retrieve pixel-by-pixel phase-shift maps (bottom left). Cellular dimensions were determined via segmentation and skeletonization (bottom right).

B) QPI phase shifts were calibrated by imaging cells in media supplemented with a range of concentrations of BSA. The retrieved phase shift is linearly related to concentration (dashed line is the linear best fit).

C) Histogram of dry-mass density measurements of exponential-phase fission yeast cells grown at 30 °C in YE5S medium. A Gaussian fit (red) yielded a mean (dashed line) density of 282±16 mg/mL (n=2345 time points, 78 cells). SD, standard deviation.

761 D) Average cell density varied by less than 10% across temperatures and temperature shifts.
762 Edges of the boxes indicate 25th and 75th percentiles, centerline is the median, and
763 whiskers indicate extreme points not considered outliers. In experiments in which the
764 temperature was shifted up, cells were initially grown at 25 °C and then moved to the
765 microscope pre-heated to the indicated temperature for long-term imaging.

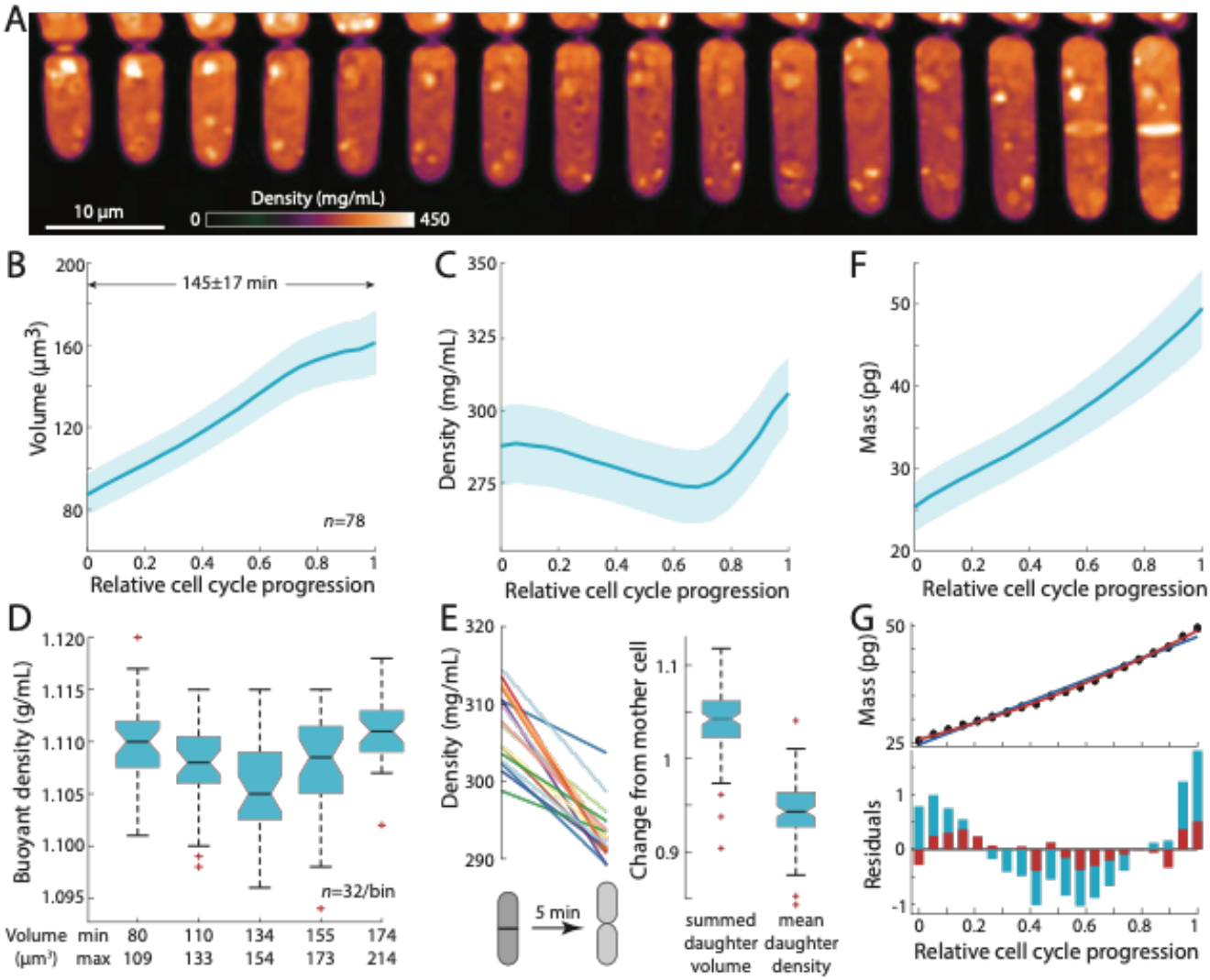

Figure 2: Intracellular density varies across the cell cycle.

A) Wild-type fission yeast cells in exponential phase were imaged in time lapse in a microfluidic chamber and phase-shift maps were extracted by QPI. Shown are images of a representative cell traversing the cell cycle from (left) cell birth to (right) septation (10 min/frame).

B,C,F) Cell volume (B), density (C), and dry mass (F) of cells aligned by their relative progression in the cell cycle. Curves are mean values and shaded regions represent 1 standard deviation (n=78 cells). Mass was estimated from volume and density measurements.

D) SMR-based measurements of fission yeast cells in an asynchronous culture (binned by cell volume) showed a similar decrease in buoyant density at intermediate volume as QPI measurements of dry-mass density (C).

E) Cell density decreases upon cell separation. Left: density measurements of cells just before and just after cell separation (5 min apart). Right: normalized changes in volume and density between the mother and resultant daughter cells.

G) Dry mass grows more exponentially than linearly. The residuals (bottom) of an exponential fit (red) to mass growth were much smaller than a linear fit (blue). See also Figure S2A.

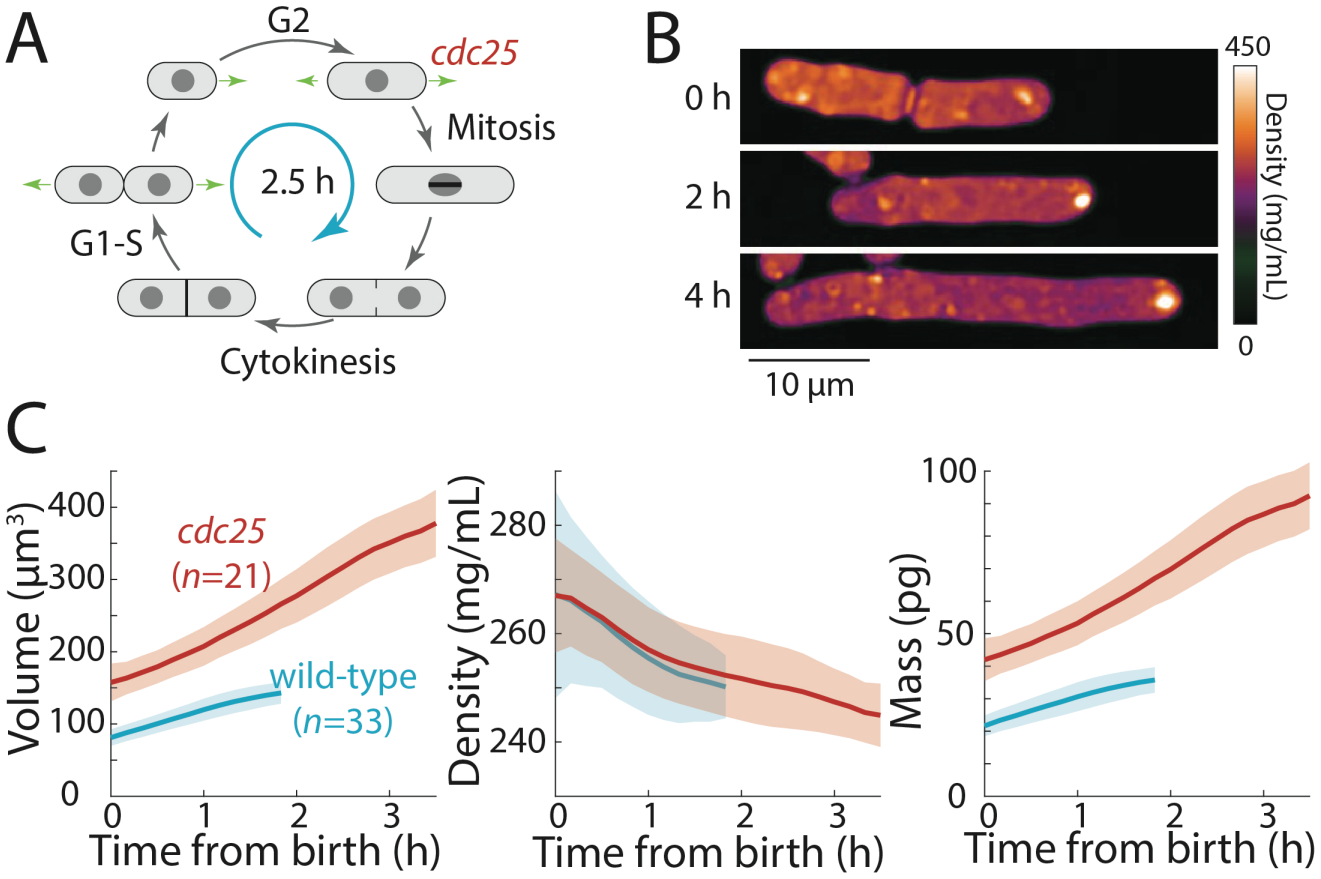

Figure 3: Extension of the G2 phase of the *S. pombe* cell cycle results in cell elongation and decreased intracellular density.

A) Schematic of the fission yeast cell cycle, highlighting the point at which the *cdc25* temperature-sensitive mutant delays the G2-M transition.

B) *cdc25-22* cells were shifted from the permissive temperature 25 °C to the semi-permissive temperature 32 °C to extend G2 phase, leading to continued cell elongation. QPI density maps of a representative cell are shown. Note that density decreased during cell elongation.

C) QPI-based measurements of volume (left), density (middle), and dry mass (right) of *cdc25-22* cells (red) that grew at least 2.5-fold relative to their birth length before dividing, compared with wild-type cells (blue) under the same conditions. Measurements are aligned from cell birth until elongation rate decreased to 20 nm/min (as an indication of the transition to mitosis). Curves are mean values and shaded regions represent 1 standard deviation.

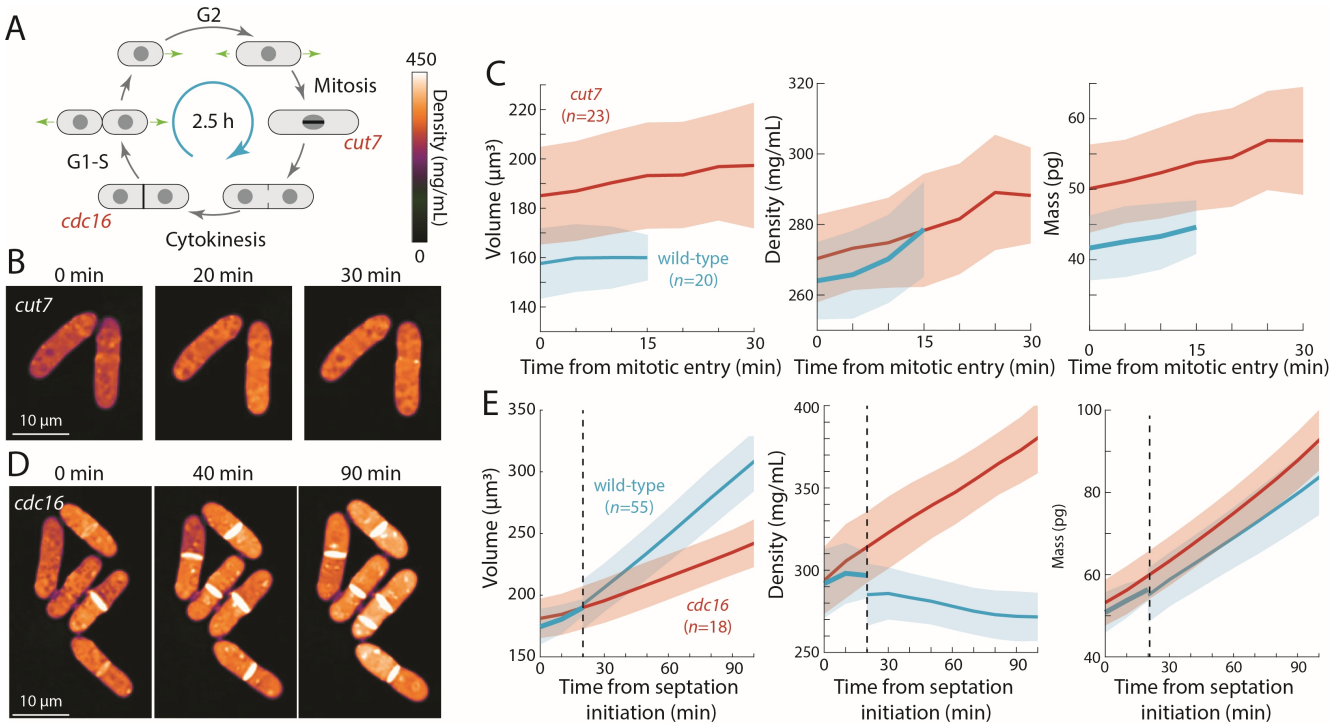

Figure 4: Cell-cycle arrests in mitosis and cytokinesis result in increased intracellular density in *S. pombe*.

A) Temperature-sensitive mutants *cut7-446* (spindle kinesin-5) and *cdc16-116* block the cell cycle in mitosis and cytokinesis, respectively.

B) *cut7-446* cells were shifted from 25 °C to 30 °C to delay mitotic progression. QPI of two representative cells delayed in mitosis for ~20 min until the onset of septation (30 min time point). Note that density continued to increase during mitotic arrest.

C) QPI-based measurements of volume (left), density (middle), and dry mass (right) of *cut7-446* cells from mitotic entry (t=0) through initiation of septum formation at cytokinesis. Curves are mean values and shaded regions represent 1 standard deviation.

D) *cdc16-116* cells were shifted from 25 °C to 34 °C to arrest cells in cytokinesis. QPI of five representative cells are shown. *cdc16* cells generally did not complete cell separation and often assembled additional septa without elongating. Note that density increased during this cytokinetic arrest.

E) QPI-based measurements of volume (left), density (middle), and dry mass (right) of *cdc16-116* cells from initiation of the first septum (t=0). Wild-type cells separated after ~20 min (dashed line), and thereafter the behavior of the daughter cells was tracked for comparison with *cdc16* cells (volume and dry mass were summed for the two daughter cells). Curves are mean values and shaded regions represent 1 standard deviation.

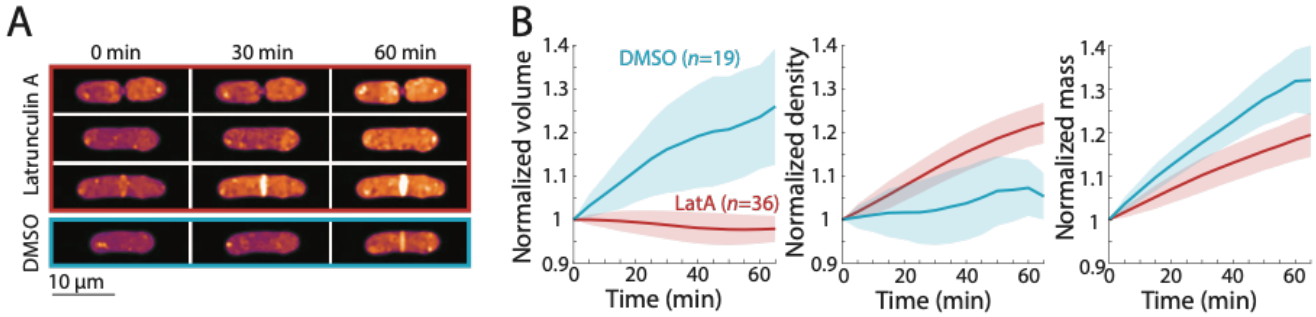

Figure 5: Cell cycle-independent growth inhibition by latrunculin A results in increased intracellular density in *S. pombe*.

A) Latrunculin A treatment inhibited cell growth and increased intracellular density regardless of cell-cycle stage. Representative QPI density maps of three wild-type cells at different points of the cell cycle treated with 200 μM latrunculin A for the indicated times. As a control, cells were treated with 1% DMSO; growth continued and density remained relatively constant.

B) QPI-based volume (left), density (middle), and dry mass (right) measurements of latrunculin A (LatA)-treated or DMSO-treated wild-type cells from the start of treatment (t=0). Growth halted and density increased due to continued mass synthesis during treatment. Curves are mean values and shaded regions represent 1 standard deviation.

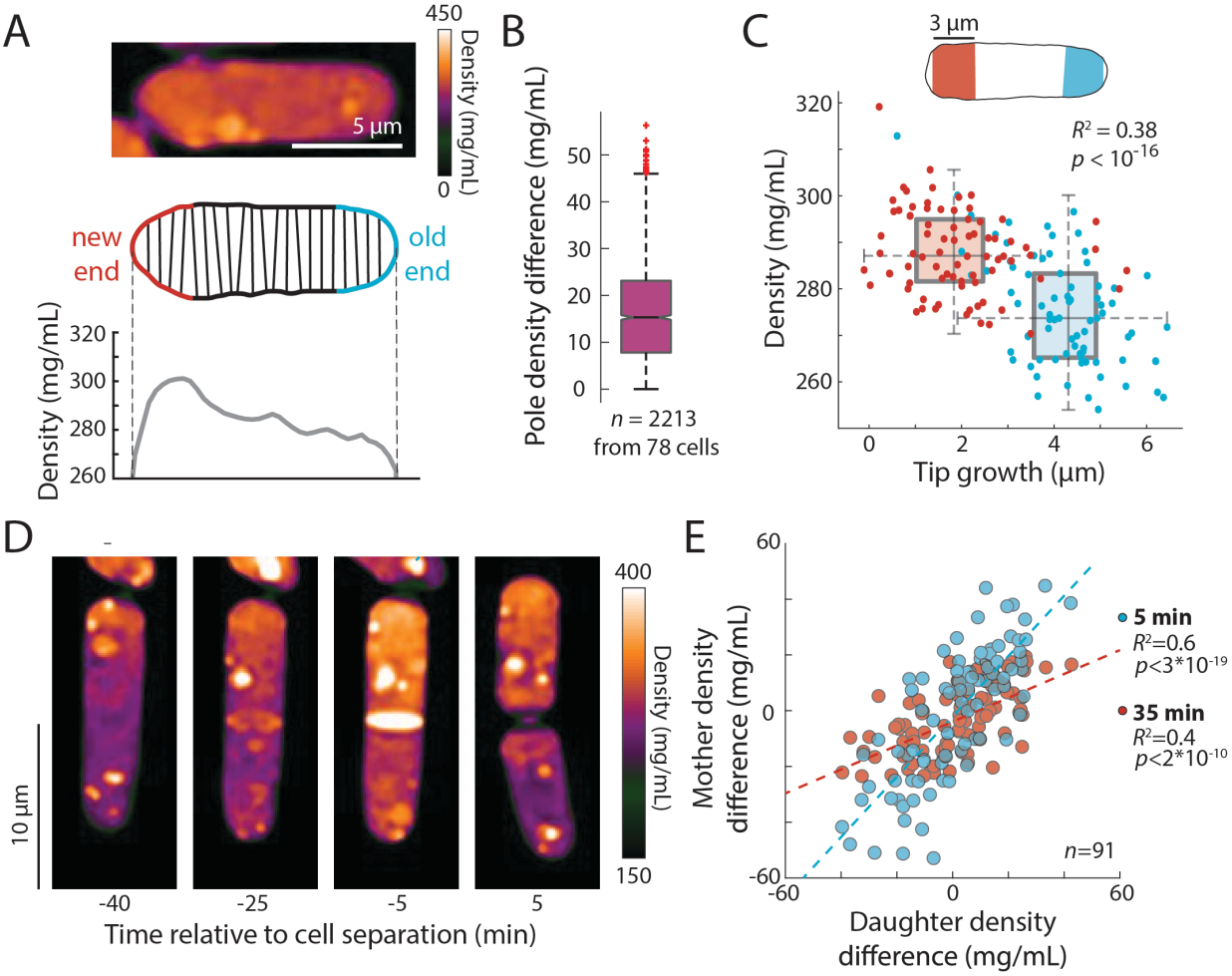

Figure 6: An intracellular density gradient negatively correlates with tip growth in *S. pombe*.

A) Top: QPI of a representative cell displaying an intracellular gradient of density. Middle: Density was measured in slices perpendicular to the long axis. Bottom: The new end (non- or slowly growing) exhibited a higher density than the old (growing) end.

B) Density was substantially different between the new and old ends in many cells. Time-lapse QPI was used to measure the densities in regions within 3 µm of each cell end. Shown is the density difference between the cell poles averaged over the cell cycle. Box extends from 25th to 75th percentile, with the median as a horizontal bar. Whiskers indicate extreme points not considered outliers (n=78 cells).

C) Mean density and amount of tip growth over an entire cell cycle was measured in 3 µm regions at the old (blue) and new (red) ends. Old ends grew more and exhibited lower mean densities over the course of the cell cycle than new ends.

D) QPI density map of a representative cell at interphase, the start of septum formation, late in septum formation, and after cell division. The gradient of intracellular density in the interphase cell was maintained over time and passed on to the daughter cells.

E) Asymmetric density patterns are propagated to the next cell cycle. The density difference between the two ends of a mother cell correlated with the density difference between the

progeny daughter cells. Shown are Pearson's correlation coefficient between the density difference of daughter cells and the corresponding halves of the mother cell at 5 min (blue) or 35 min (red) before cell division. The halves of the mother cell exhibited a larger range of density differences at the later time point, when they were more consistent with the density differences between daughter cells.

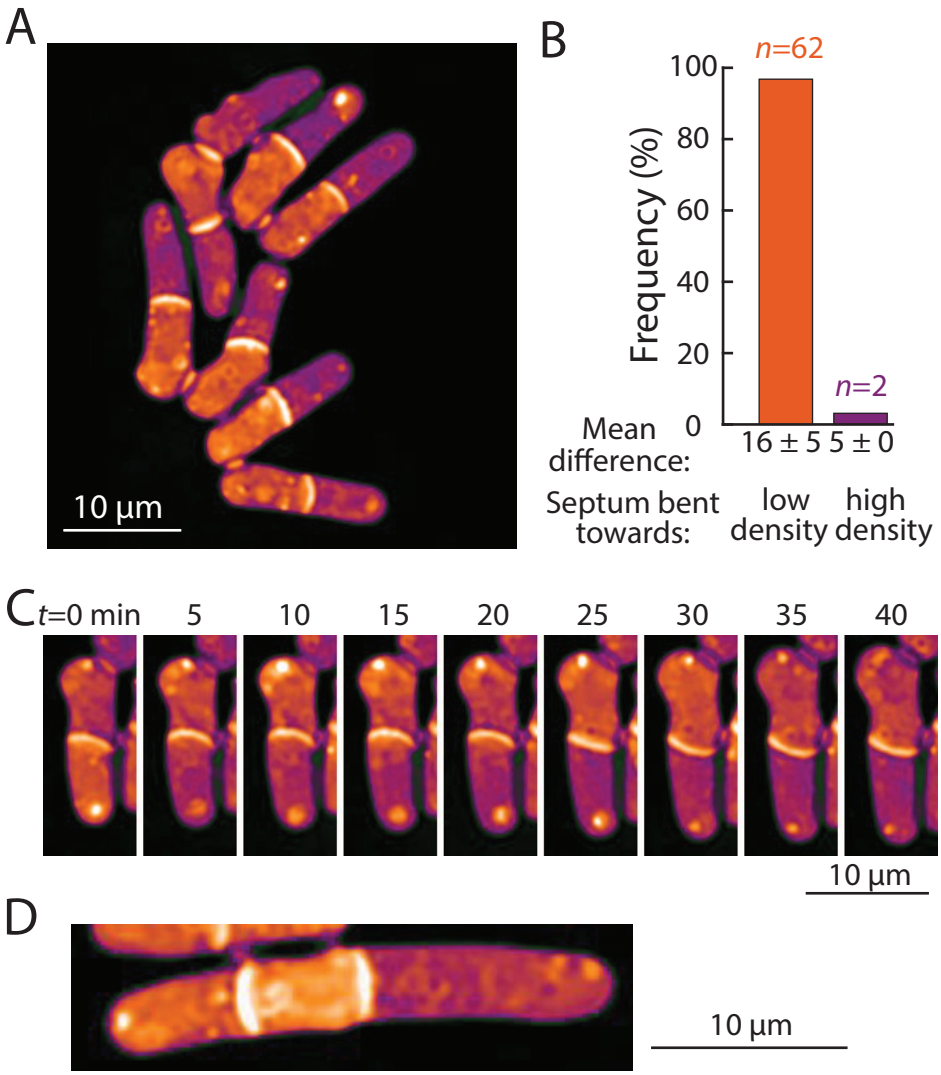

Figure 7: Bending of the septum reveals a link between intracellular density and osmotic pressure.

A) QPI density map of *mid2Δ cells* that are delayed in cell separation showed bent septa and density differences between two daughter-cell compartments. Note that the septa are bent away from the denser compartment in all cells in this image.

B) The direction of septum bending was almost always toward the lower-density daughter cell. The direction of the bent septum was measured at the time of maximum density difference between daughter-cell compartments.

C) An example of a cell in which the direction of septal bending and the sign of the density difference between daughter-cell compartments fluctuated over time. After the bottom compartment decreased and the top compartment increased in density, the septum bent in the opposite direction, consistent with the correlation between bending and density difference in (B).

870 D) In multi-septated *mid2Δ* cells, internal compartments bounded by two septa exhibited
871 higher density than the surrounding compartments; in these situations, both septa
872 typically bent away from the higher-density compartment.

873 **Supplemental Table**

874

875 **Table S1: *S. pombe* strains used in this study.**

Genotype	Strain number	Source
h- wild-type strain 972	FC15	Chang lab
h- cdc25-22	FC342	Chang lab
h- cut7-446 leu1-32	FC1455	Chang lab
h- cdc16-116	FC13	Chang lab
h- mid2::kanMX ade6 leu1-32 ura4-D18	FC881	Chang lab

876

877 **Supplemental Figures**

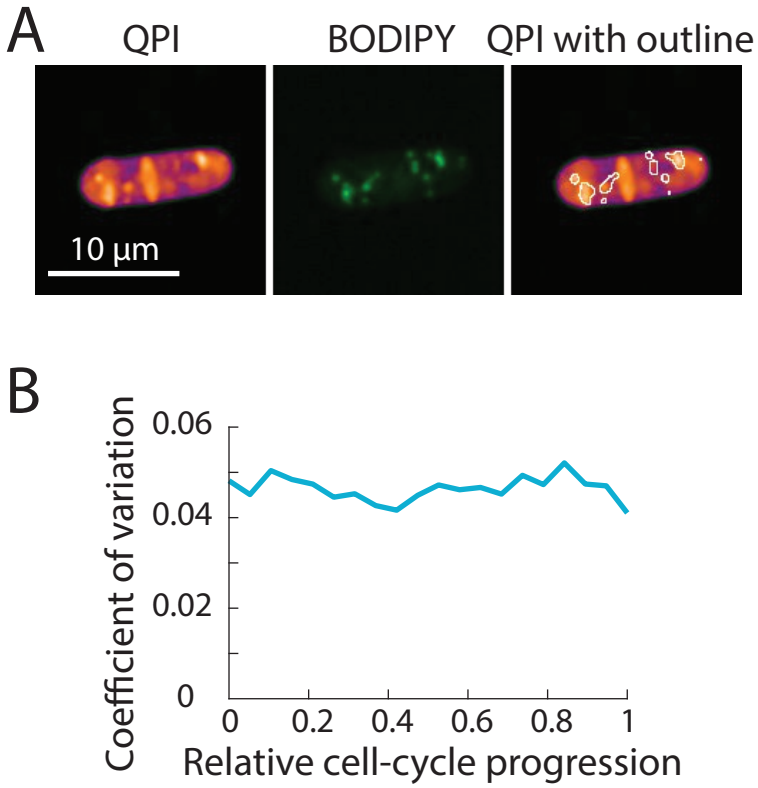

878

879 **Supplemental Figure 1: High-density features in QPI co-localize with lipid droplets.**

880 A) Cells were stained with BODIPY dye to identify lipid droplets. QPI density map (left) and
881 the corresponding fluorescence image of a representative BODIPY-stained wild-type
882 fission yeast cell (middle). The fluorescence intensity image was thresholded to identify
883 regions containing lipid droplets (outlines), which overlapped with high-density regions
884 in QPI (right).

885 B) Coefficient of variation (CV) of intracellular density over the cell cycle. The CV at each
886 specific stage of cell-cycle progression (<5%) was slightly lower than the CV across an
887 entire cell population (6%, Figure 1C), supporting the notion that some population-wide
888 variation arises from cell cycle-dependent density variations.

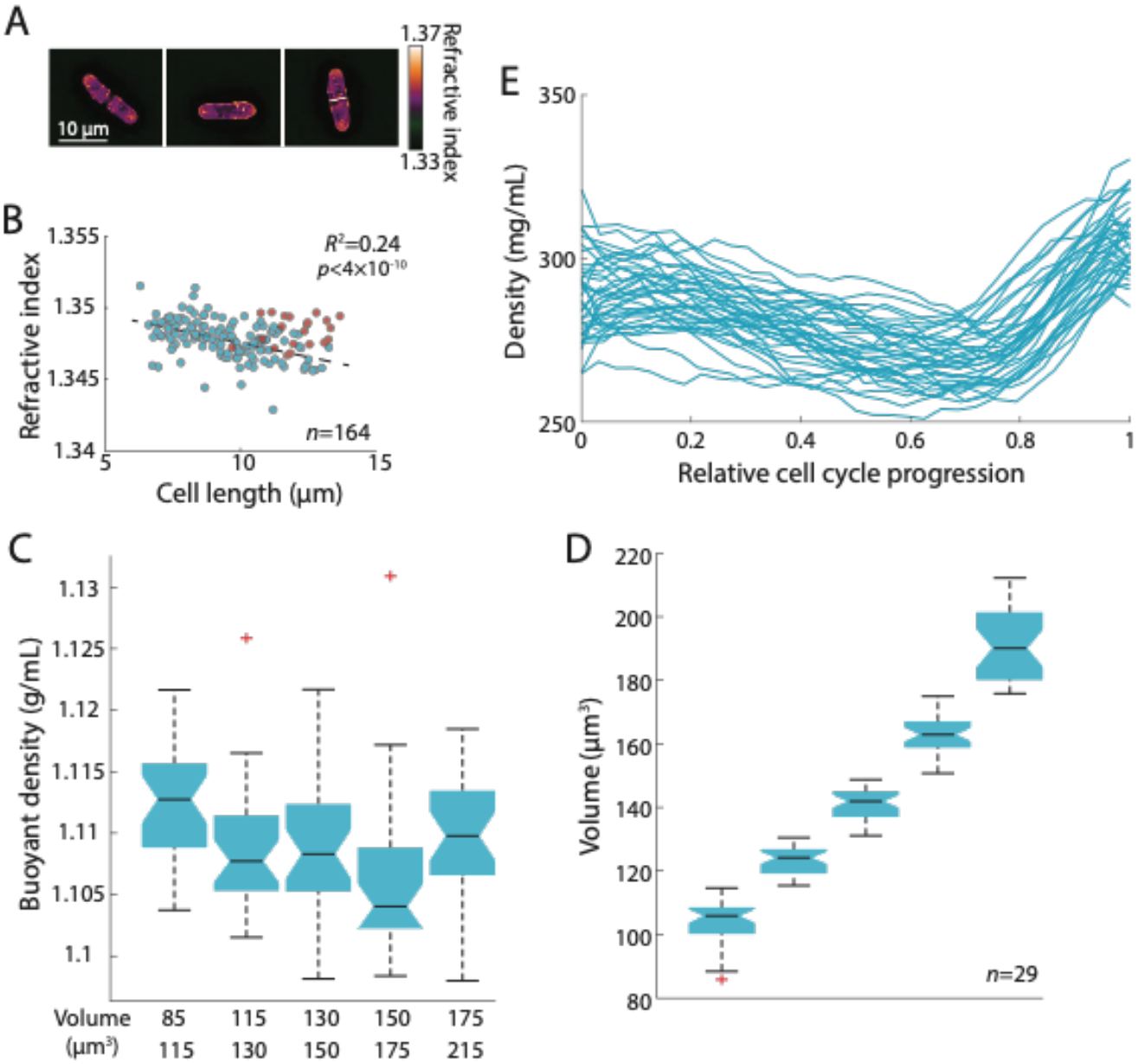

Supplemental Figure 2: Measurements of buoyant density and buoyant mass using SMR and refractive index measurements using holography and QPI show cell cycle-dependent density variations.

A) Representative holographic images of cells at an early, middle, and late stage in the cell cycle.

B) Mean refractive index was calculated from holographic images of non-septated cells (blue) and septated cells (red). The negative correlation (Pearson's correlation coefficient) of refractive index with non-septated cells (dashed line) indicates that refractive index decreases with increasing cell length.

C) Replicate SMR experiment for data in Figure 2D. Medium-sized cells exhibited lower buoyant density than small and large cells, similar to QPI measurements (Figure 2C).

Boxes indicate 25th and 75th percentiles and horizontal line indicates the median. Whiskers indicate the most extreme datapoints not considered outliers.

D) Distribution of the volumes of cells in each bin of the buoyant density measurements in (C). Each bin contains 29 cells sorted by volume.

E) QPI-based dry-mass density measurements of individual cells showed similar variation throughout the cell cycle as the population (Figure 2C).

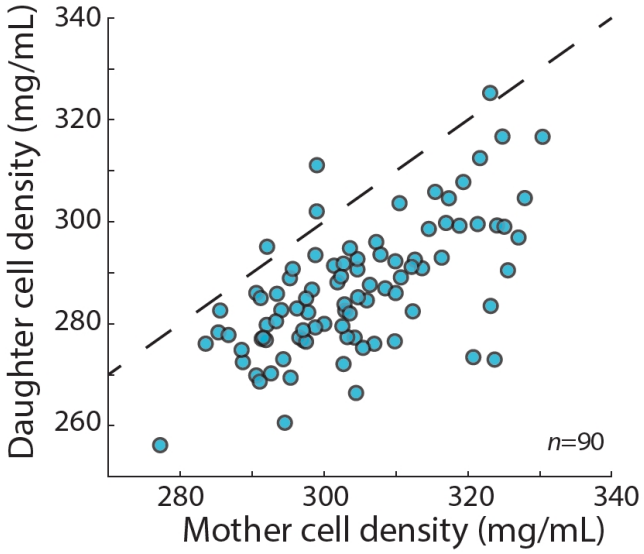

Supplemental Figure 3: The mean density of *S. pombe* daughter cells was typically lower than the density of the mother cell.

The densities of the mother cell and the associated daughter cells were measured from consecutive QPI density maps (5 min apart) directly before and after cell division, respectively. The daughter cell densities were then averaged. In large majority of cases, the newly born daughter cells were less dense than the mother cell 5 min beforehand. Dashed line indicates $y=x$.

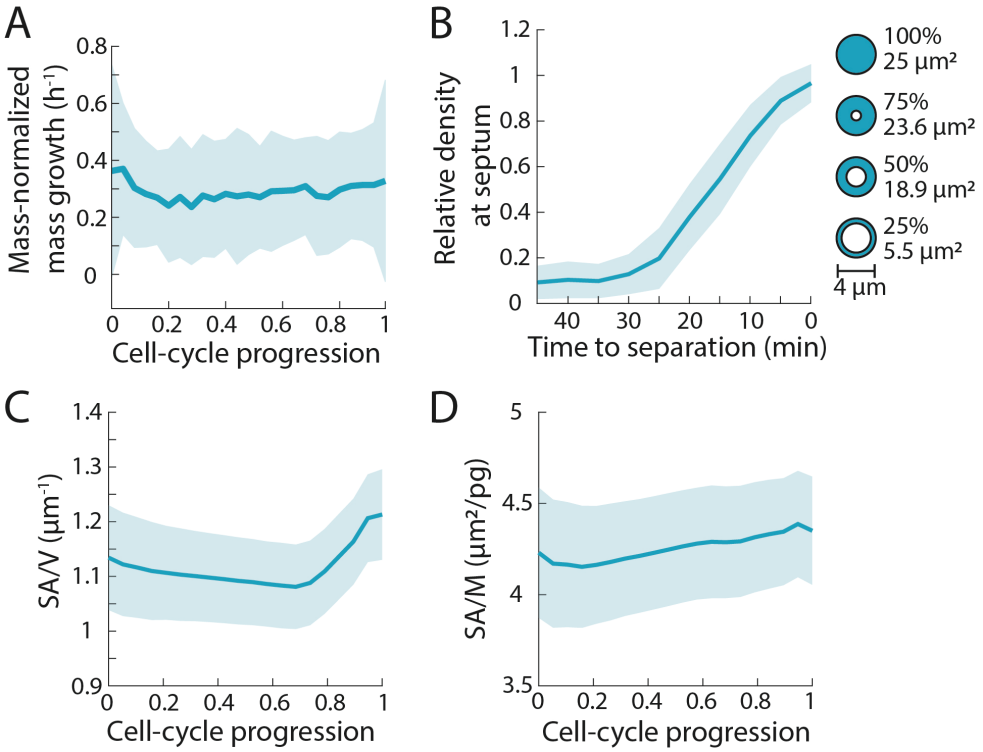

Supplemental Figure 4: Cellular surface area-to-mass ratio varies less than dry-mass density during the *S. pombe* cell cycle.

A) Mass increases exponentially throughout the cell cycle, as evidenced by the constant rate of normalized growth ($1/M\ dM/dt$). The dry mass of individual cells was measured as in Figure 2. Larger cells added more mass per unit time, a characteristic of exponential mass growth. Curves are mean values and shaded regions represent 1 standard deviation (n=78 cells).

B) To measure surface area, we took into account the surface area added at the septum during cytokinesis. Septum growth was estimated by measurement of density at the septal region prior to division. The surface area of the septum was calculated by assuming a double-layered structure with a diameter of 4 µm. The local density was used to estimate the diameter of the opening, such that at 50% of maximal density, 50% of the cross-sectional diameter was assumed to be filled with septal wall. Curves are mean values and shaded regions represent 1 standard deviation (n=78 cells).

C) Surface area to volume (SA/V) ratio increased at the end of the cell cycle, as volume growth slowed and surface area increased due to septum formation. Curves are mean values and shaded regions represent 1 standard deviation (n=78 cells).

D) Surface area to mass (SA/M) ratio varied by only ~5%. Curves are mean values and shaded regions represent 1 standard deviation (n=78 cells). Thus, SA/M shows less variation than the ratio of volume to mass (the inverse of density).

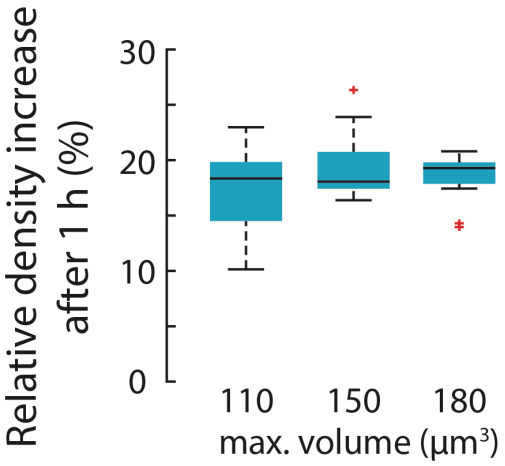

935

936 **Supplemental Figure 5: The increase in intracellular density due to treatment with the**
937 **actin inhibitor latrunculin A was not dependent on cell size.**
938 Wild-type *S. pombe* cells were treated with 0.2 mM latrunculin A for 1 h and density maps were
939 measured using QPI as in Figure 6. Density increase over 1 h normalized to mean density at the
940 first time point was approximately invariant across initial cell sizes. Cells per bin, left to right: 10,
941 10, 12. Boxes indicate 25th and 75th percentiles and horizontal line indicates the median.
942 Whiskers indicate the most extreme datapoints not considered outliers.

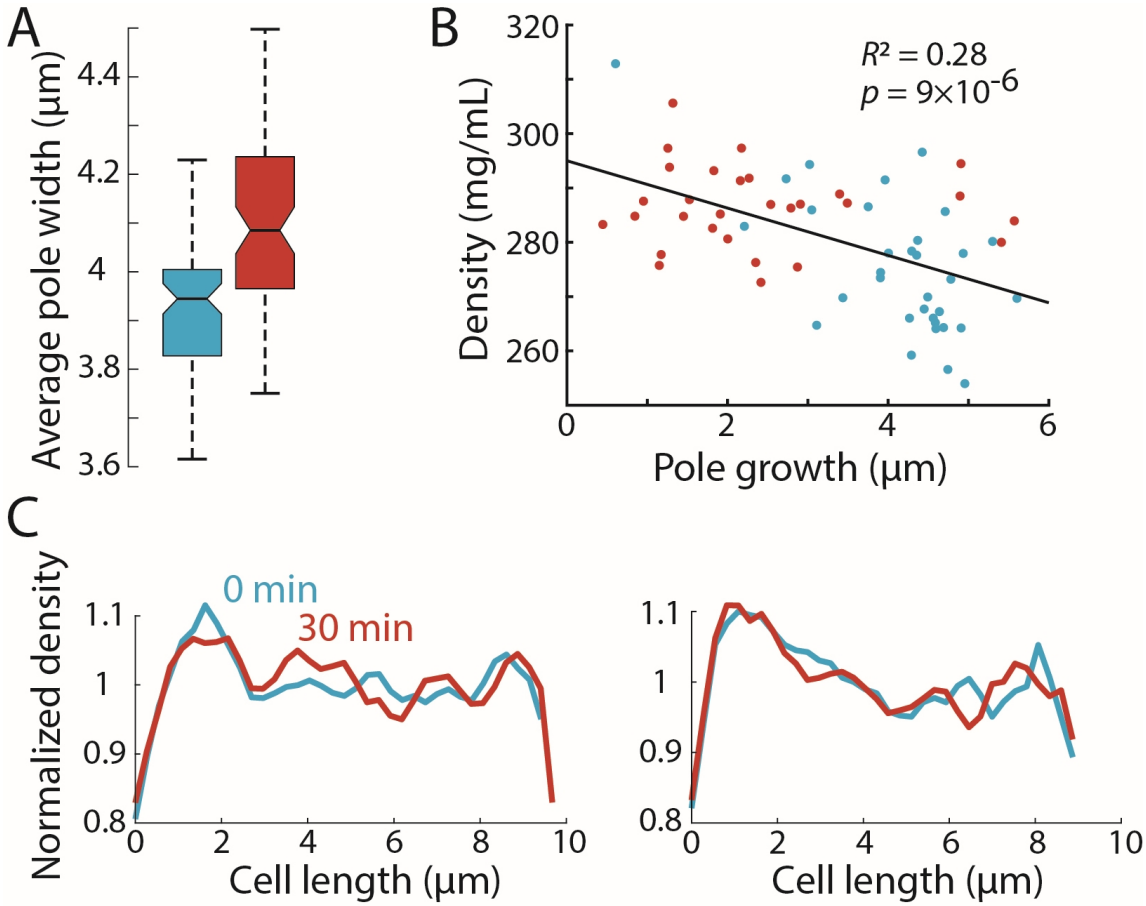

Supplemental Figure 6: Spatial intracellular density gradients are present in cells with similar widths, and are stably maintained in cells treated with latrunculin A.

A) The new cell end is wider than the old end. The mean width of the region 1.5-3 μm away from the cell pole was extracted for the new and old ends over time and averaged. The average old end width was ~0.15 μm smaller than that of new ends. Boxes indicate 25th and 75th percentiles and horizontal line indicates the median.

B) To address a caveat that differences in QPI density maps may arise from differences in cellular height, we restricted our measurements of average pole density to poles with similar widths (between 3.9 and 4.1 μm, corresponding to the medians in (A)). Tip growth through the cell cycle and average density at the ends were plotted as in Figure 3C. The negative correlation (Pearson's correlation coefficient) between pole growth and density observed in Figure 3B persisted, suggesting that the difference in measured density between poles is not due to differences in sample height.

C) The density gradient was stable in latrunculin A-treated cells. Cells were treated with latrunculin A and imaged using QPI as in Figure 5. Normalized QPI density plots along the long axis of two individual cells before and 30 min after treatment with latrunculin A. The density gradient was maintained in the absence of F-actin and tip growth.

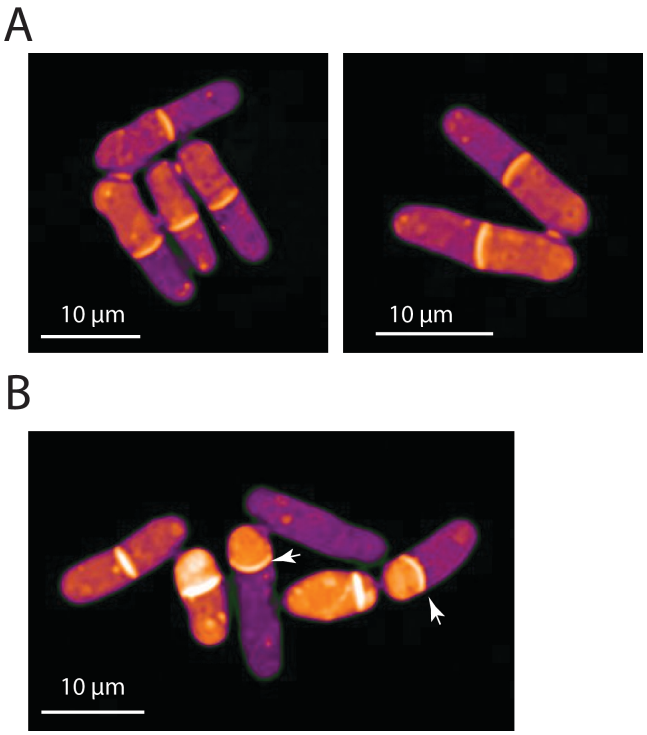

Supplemental Figure 7: Septa bend away from the compartment of higher density in *mid2* and *cdc16* mutant cells.

A) QPI density maps of *mid2Δ* cells delayed in cell separation often exhibited differences in density between sister-cell compartments, and in most cases the septum was bent away from the compartment of higher density.

~~B)~~ QPI density map of *cdc16* cells grown at 25 °C and then imaged on a microscope pre-heated to 34 °C; image shows *t*=3 h time point. These cells often exhibited an asymmetrically positioned septum, which formed a small cellular compartment that did not grow much and increased in density and septum bending (arrows).